Hydrothermal, multiphase convection of H2O-NaCl fluids from ambient to magmatic temperatures

A new numerical scheme and benchmarks for code comparison

Journal Article

Author(s):
Weis, Philipp; Driesner, Thomas; Coumou, Dim; Geiger, Sebastian

Publication date:
2014-08

Permanent link:
https://doi.org/10.3929/ethz-b-000081941

Originally published in:
Geofluids 14(3), https://doi.org/10.1111/gfl.12080

This is the Green Open Access version of Weiss, P., Driesner, T., Coumou, D. and Geiger Sebastian, 2014. Hydrothermal, Multi-phase Convection of H_2O-NaCl Fluids from Ambient to Magmatic temperatures: a new Numerical Scheme and Benchmarks for Code Comparison. *Geofluids,* vol. 14, pp. 347-371.
Original publication see: https://doi.org/10.1111/gfl.12080

Hydrothermal, Multi-phase Convection of H_2O-NaCl Fluids from Ambient to Magmatic Temperatures: A new Numerical Scheme and Benchmarks for Code Comparison

Philipp Weis[1*], Thomas Driesner[2], Dim Coumou[3] and Sebastian Geiger[4]

[*]Corresponding Author
[1] Institute of Geochemistry and Petrology, ETH Zurich
Clausiusstrasse 25 (NW F 84), 8092 Zürich, Switzerland
Phone +41 44 632 0483, Fax +41 44 632 1827, e-mail: philipp.weis@erdw.ethz.ch

[2] Institute of Geochemistry and Petrology, ETH Zurich
Clausiusstrasse 25 (NW F72), 8092 Zürich, Switzerland
Phone +41 44 632 68 03, Fax +41 44 632 18 27, email thomas.driesner@erdw.ethz.ch

[3] Earth System Analysis, Potsdam Institute for Climate Impact Research
Telegrafenberg A62/0.04, P.O. Box 60120, 14412 Potsdam, Germany
Phone +49 331 288 2442, Fax +49 331 288 2680, e-mail: coumou@pik-potsdam.de

[4] Institute of Petroleum Engineering, Heriot-Watt University
Edinburgh EH14 4AS, United Kingdom
Phone +44 131 451 8054, Fax +44 131 451 3127, e-mail: sebastian.geiger@pet.hw.ac.uk

Abstract

Thermohaline convection of subsurface fluids strongly influences heat and mass fluxes within the Earth's crust. The most effective hydrothermal systems develop in the vicinity of magmatic activity and can be important for geothermal energy production and ore formation. As most parts of these systems are inaccessible to direct observations, numerical simulations are necessary to understand and characterize fluid flow. Here, we present a new numerical scheme for thermohaline convection based on the Control Volume Finite Element Method, allowing for unstructured meshes, the representation of sharp thermal and solute fronts in advection-dominated systems and phase separation of variably miscible, compressible fluids. The model is an implementation of the Complex System Modeling Platform CSMP++ and includes an accurate thermodynamic representation of strongly non-linear fluid properties of salt water for magmatic-hydrothermal conditions (up to 1,000 °C, 500 MPa and 100 wt% NaCl). The method ensures that all fluid properties are taken as calculated on the respective node by using a fully upstream-weighted approach, which greatly increases the stability of the numerical scheme. We compare results from our model with two well-established codes, HYDROTHERM and TOUGH2, by conducting benchmarks of different complexity and find good to excellent agreement in the temporal and spatial evolution of the hydrothermal systems. In a simulation with high-temperature, high-salinity conditions currently outside of the range of both HYDROTHERM and TOUGH2, we show the significance of the formation of a solid halite phase, which introduces

heterogeneity. Results suggest that salt added by magmatic degassing is not easily vented or accommodated within the crust and can result in dynamic, complex hydrologies.

1. Introduction

Thermohaline convection of fluids in the subsurface plays a leading role in many hydrological and geological processes (Ingebritsen et al. 2006), forming hydrothermal systems that can be of significant economic importance for georesources such as geothermal energy or mineral deposits (Kesler 1994). Gradients in temperature, salinity and fluid pressure are the driving forces for thermohaline convection and are strongest in the vicinity of magmatic activity in the Earth's upper crust. With the emplacement of shallow magma chambers, fluids at ambient temperatures as determined by the geothermal gradient can be exposed to magmatic temperatures of more than 1,000°C. Depending on the size of the magma chamber, magmatic-hydrothermal systems can influence the hydrology over several kilometers laterally and vertically. The relevant processes take place on multi-millennia timescales. This combination of extreme conditions at depth, large size, and long lifetimes excludes direct observation as means for a comprehensive understanding of such systems. Therefore, numerical simulations are an important method that allows us to understand and characterize fluid flow and its interaction with the rock in magmatic-hydrothermal systems (Ingebritsen et al. 2010) and the considerable variation between different geological settings.

Hydrothermal systems at divergent plate margins present the volumetrically most abundant and effective form of thermohaline convection, accounting for 25 % of the global heat flux from the Earth's interior to the surface (Stein and Stein 1994). At mid-ocean-ridges, magmatism is predominantly basaltic, with a relatively low water content, and mainly acts as a heat source for the convection of seawater that percolates through the ocean floor into the crust and returns to the ocean at black smoker vent fields (Halbach 2003).

Tectonic activity at convergent plate margins produces more hydrous magmas. Melts generated during the subduction process rise through the lithosphere and may eventually get trapped at shallow, upper-crustal levels. During crystallization, these magma chambers also release magmatic volatiles because the initial melt was able to dissolve more water than can be incorporated in the solidified rock. These magmatic fluids are released into the overlying host rock, displacing or mixing with the ambient waters in the pore space. Hydrothermal veins and breccias in fossil magmatic settings and seismic activity at active hydrothermal systems show that elevated fluid pressures can lead to rock failure (Cox 2005). Fluid inclusion analyses in ore-forming systems and observations at high-enthalpy geothermal systems show that fluid pressures can locally and temporarily rise to near-lithostatic values (Fournier 1991; Rusk et al. 2004).

Salts such as NaCl and other metal chlorides strongly influence fluid flow as they widen the field of vapor-liquid coexistence to much higher temperatures and pressures as compared to pure water (Driesner and Heinrich 2007) (Figure 1). The presence of evaporite layers in the host rock stratigraphy can increase salinity through dissolution by the convecting fluids. Submarine magmatic-hydrothermal systems at mid-ocean ridges and submerged volcanoes contain fluids of seawater salinity of about 3.2 wt% NaCl and magmatic volatiles released at arc volcanic settings contain several wt% NaCl (Cline and Bodnar 1991). Initially moderate salinities can also locally increase to much higher values if fluids phase-separate into high-salinity, high-density brines and low-salinity, low-density vapors that flow with different velocities after separation. Fluids can also locally saturate in solid halite (Cloke and Kesler 1979).

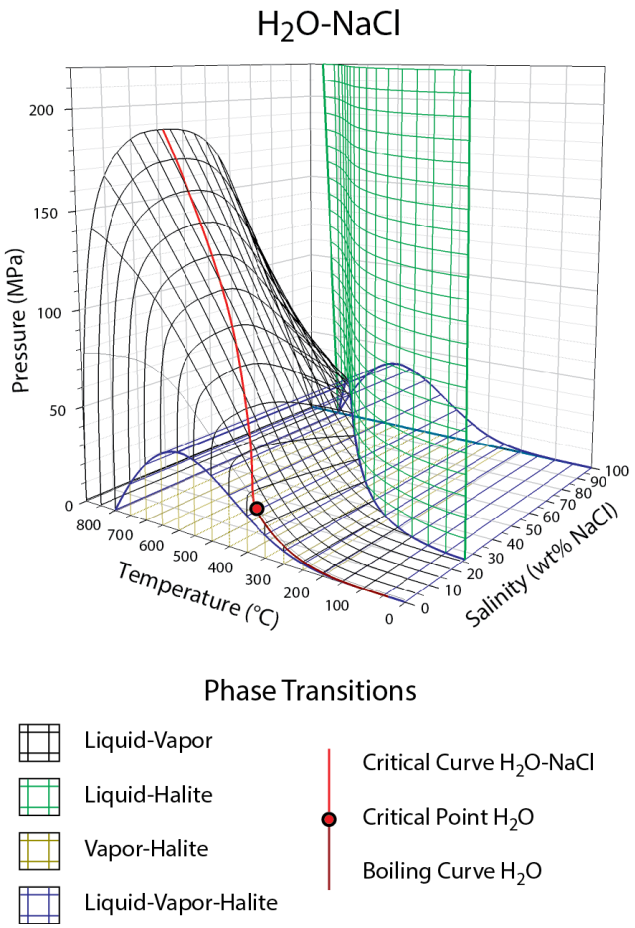

Figure 1. Phase diagram of the H2O-NaCl System. The black tunnel-shaped surface shows the phase transition from a single-phase fluid at high-temperature, high-pressure conditions to a two-phase coexistence of liquid and vapor at conditions within the black tunnel. The green curtain-shaped surface shows the transition from a single-phase fluid with dissolved salt to a salt-saturated liquid; at conditions behind the curtain liquid coexists with solid halite. The blue carpet-shaped surface marks the three-phase coexistence of vapor, liquid, and halite. The beige-colored surface below this carpet indicates the coexistence of vapor and halite. The dark red line shows the boiling curve of H2O, which ends in the critical point of H2O at 374°C and 21.1 MPa. The critical curve of the H2O-NaCl system (red line) is the crest of the liquid–vapor coexistence field (modified from Driesner & Heinrich 2007).

Apart from magmatic processes, gradients driving thermohaline convection can also arise naturally from lithological contrasts, e.g. at the interface of rock units with different permeability (Ingebritsen et al. 2006). Hydrological differences induce gradients where fluids from different reservoirs interfere, such as basinal brines with low-salinity groundwater (Kesler 1994). Topographical differences can induce fluid flow by introducing horizontal pressure gradients, wheras pressure perturbations by metamorphic devolatilization and earthquakes are other natural drivers or triggers for subsurface fluid flow (Sammel et al. 1988; Sibson 1992; Connolly and Podladchikov 2004; Bani-Hassan et al. 2012). Thermohaline convection can also be stimulated by injection or withdrawal of fluids through wells (e.g. Gunnarsson et al. 2011). In enhanced geothermal (or petrothermal) systems, cold fluid is injected to increase fluid pressure in order to stimulate failure of fractures to enhance permeability (Evans et al. 2005; Fairley et al. 2010).

Numerical simulations of thermohaline convection in general – and of magmatic-hydrothermal systems in particular – require an approach that can represent fluid properties of salt water from ambient to magmatic temperatures and lithostatic pressures in the upper crust and handle strong

gradients and large source terms. There are several existing flow codes and their approaches and capabilities have been the subject of a recent review (Ingebritsen et al. 2010). However, most codes are still of limited applicability to magmatic-hydrothermal systems. HYDROTHERM, a finite difference code provided and maintained by the USGS, can handle high temperatures and pressures but is limited to fluid properties of pure water (Kipp et al. 2008). Further, although the finite difference method can be refined locally, the structural mesh imposes constraints on the spatial discretization. The FEHM code can simulate hydrothermal convection of pure water using the finite element method (e.g. Keating et al. 2002). Other approaches combine the finite element method with a node-based semi-Lagrangian advection scheme (Bani-Hassan et al. 2012). TOUGH2 includes salt water but is limited to temperatures up to 350°C (Pruess 2004). It uses an integrated finite difference method (IFD) to discretize the governing equations in space.

Several efforts have been initiated to overcome these limitations. A subversion of the TOUGH-family of models, TOUGH-NaCl, is extending the range to higher temperatures (Kissling 2005b; Kissling 2005a). The CSMP++ code uses a combined finite element finite volume (FEFV) approach on unstructured grids and can treat salt water up to magmatic temperatures (Geiger et al. 2006a; Geiger et al. 2006b; Coumou 2008; Coumou et al. 2009). The FISHES code solves for thermohaline convection on structured meshes with a finite volume approach (Lewis and Lowell 2009).

The major challenge of numerical simulations of thermohaline convection is the treatment of the highly non-linear fluid properties and phase separation. These transiently evolving non-linearities are introduced as coefficients to advection-diffusion type equations. Here, we present an implementation of the Control Volume Finite Element Method (CVFEM) to solve for mass and heat transport in porous media. This transport code has been built within the Complex System Modeling Platform CSMP++ (Matthai et al. 2007) and is coupled to an accurate thermodynamic model for H_2O-NaCl fluids (Driesner 2007; Driesner and Heinrich 2007).

As analytical solutions are limited for these non-linear systems, benchmarking studies and inter-code comparisons are essential to increase our confidence in the existing numerical models and have been called for in a recent review paper (Ingebritsen et al. 2010) and a white paper by the International Partnership for Geothermal Technology (IPGT; Ketilsson et al. 2012). We compare our simulations with the results of two other well-established models, namely HYDROTHERM (Kipp et al. 2008) and TOUGH2 (Pruess 1991; Pruess 2004). We further show an example of a high-temperature, high-salinity flow system that is currently outside of the range of these two models.

While our new numerical method was tailored to ensure stable solutions in regions with strong gradients, highly non-linear fluid properties, phase transitions and large source terms, as required for simulations of magmatic-hydrothermal systems, it can also be applied to a wide range of less drastic hydrological settings. Here, however, we focus on the dynamics and numerical implementation of multi-phase flow of H_2O-NaCl fluids at magmatic-hydrothermal conditions.

2. Method

2.1 Continuum Porous Medium Approach

For large scale description of upper crustal hydrology, fluid flow and heat transport through porous and fractured rocks can be described with a continuum porous medium approach based on the extended form of Darcy's Law, where

$$v_i = -k\frac{k_{ri}}{\mu_i}\left(\nabla p - \rho_i g\right) \qquad i = \{v, l\} \tag{1}$$

is the Darcy velocity v of phase i, k denotes permeability, k_r relative permeability, μ dynamic viscosity, p total fluid pressure, ρ fluid density, and g acceleration due to gravity (Ingebritsen et al. 2006). The simulated fluid is a mixture of H_2O and NaCl that can separate into up to three coexisting phases vapor *v,* liquid *l*, and solid halite *h* – depending on phase relations determined by temperature and/or enthalpy, pressure and salinity (TPX and HPX; Figure 1).

In the flow equations, solid halite is considered to be immobile and acts as part of the rock as it reduces pore space, while in the mass and salt conservation equations it is treated as an (immobile) part of the NaCl component of the fluid phase. We generally use a linear relative permeability model with a residual saturation of $R_l = 0.3\left(1 - S_h\right)$ for the liquid phase, $R_v = 0.0$ for the vapor phase and $k_{rv} + k_{rl} = 1 - S_h$, where S is the volumetric saturation. This model implies that there is little interaction between the liquid and vapor phase (Wang and Horne 2000; Ingebritsen et al. 2010). However, any relative permeability model can be applied within the presented scheme (e.g. Brooks and Corey 1964).

2.2 Mass and Energy Conservation

The numerical method ensures conservation of mass, energy and solute (in this case salt). Conservation of fluid mass is obtained by

$$\frac{\partial\left(\phi\left(S_l\rho_l + S_v\rho_v + S_h\rho_h\right)\right)}{\partial t} = -\nabla\cdot\left(v_l\rho_l\right) - \nabla\cdot\left(v_v\rho_v\right) + Q_{H_2O+NaCl}\,, \tag{2}$$

with the porosity ϕ, the time t, and a source term $Q_{H_2O+NaCl}$.

Conservation of salt mass is computed as

$$\frac{\partial\left(\phi\left(S_l\rho_l X_l + S_v\rho_v X_v + S_h\rho_h X_h\right)\right)}{\partial t} = -\nabla\cdot\left(v_l\rho_l X_l\right) - \nabla\cdot\left(v_v\rho_v X_v\right) + Q_{NaCl}\,, \tag{3}$$

with X denoting the mass fraction of NaCl in the phase indicated and a source term Q_{NaCl}.

Conservation of energy accounts for heat conduction and advection and is described by

$$\frac{\partial\left[\left(1-\phi\right)\rho_r h_r + \phi\left(S_l\rho_l h_l + S_v\rho_v h_v + S_h\rho_h h_h\right)\right]}{\partial t} = \nabla\cdot\left(K\nabla T\right) - \nabla\cdot\left(v_l\rho_l h_l\right) - \nabla\cdot\left(v_v\rho_v h_v\right) + Q_e\,, \tag{4}$$

with the subscript r indicating the rock, h_i denoting the specific enthalpy of the phase indicated, thermal conductivity K, temperature T, and a source term Q_e.

Depending on the specific problem to solve, further terms might be needed. For example, diffusion and dispersion of salt could be added to the salt conservation equation (Geiger et al. 2006a; Coumou et al. 2009). Capillary effects are not explicitly calculated but could be added as another

non-linear diffusion equation using variable switching (Annewandter et al. 2013). Potential and kinetic energies are currently ignored as they are expected to be of minor importance for most systems (Faust and Mercer 1979). Given the strong pressure, temperature, and compositional gradients within magmatic-hydrothermal systems – the main objective for this numerical scheme – this set of conservation equations will describe fluid flow reasonably well in most instances.

2.3. Fluid Properties

Given the conservation equations (Eqns, 2, 3 and 4), the simulated fluid is characterized by its specific enthalpy, salinity, and pressure (HPX formulation). However, the thermodynamic model for the system H_2O-NaCl is commonly formulated in terms of temperature, pressure and salinity (TPX formulation; Figure 1). Therefore, the exact temperature of the rock and fluid in the control volume has to be calculated in a thermal equilibration step by numerical iteration. The thermodynamic model covers conditions relevant for magmatic-hydrothermal systems with temperatures up to 1000°C, fluid pressures of up to 500 MPa, and salinities of 0 to 100 wt% NaCl. The properties in the pure H_2O limit are taken from the IAPS-84 equation of state (Haar et al. 1984) and the effect of adding NaCl is described by the model of Driesner and Heinrich (2007) and Driesner (2007). These fluid properties include the values required by Equations 1 to 4: ρ_i, μ_i, h_i, X_i and S_i for the individual phases $i = \{l, v, h\}$ and the bulk fluid $i = f$.

The model also provides the isenthalpic compressibility of the fluid

$$\beta_f = \frac{1}{\rho}\left(\frac{\partial \rho}{\partial p}\right)_{HX}, \tag{5}$$

describing the density change with pressure at constant bulk enthalpy and salinity. In the two- and three-phase cases, we apply adapted versions of the isenthalpic compressibility as described in Grant and Sorey (1979), which results in values that can be orders of magnitude higher than the single-phase compressibilities, because changes in the bulk density can easily be accommodated by changing the phase proportions of the liquid and vapor phases via condensation or evaporation.

2.4. Thermal Evolution and Operator Splitting

In the geological settings of interest, the mass of rock in a given control volume is much greater than the mass of the fluid, as porosities usually have low values and the density of the rock typically is at least two to three times larger than the density of the fluid. Heat transfer by conduction will therefore be almost entirely within the rock mass, whereas heat transfer by advection happens exclusively by fluids. Hence, the advection-diffusion-type equation of energy conservation (Eqn 4) can be split into a parabolic diffusion and a hyperbolic advection part (Geiger et al. 2004; Geiger et al. 2006a; Helmig et al. 2013).

Diffusion of heat in the rock is calculated as

$$\left(1-\phi\right)\frac{\partial H_r}{\partial t} = \left(1-\phi\right)\rho_r c_{pr}\frac{\partial T}{\partial t} = \nabla\cdot\left(K\nabla T\right) + Q_c, \tag{6}$$

with the enthalpy of the rock H_r, the rock's specific heat capacity c_{pr} and a heat source term Q_c. The implementation could be adjusted to also account for heat conduction through the fluid by an appropriate averaging of thermal conductivity and heat capacity.

Advective heat transport by the fluid f is calculated as

$$\phi \frac{\partial H_f}{\partial t} = -\nabla \cdot \left(v_l \rho_l h_l \right) - \nabla \cdot \left(v_v \rho_v h_v \right) + Q_a , \tag{7}$$

with the energy stored in the fluid $H_f = S_l \rho_l h_l + S_v \rho_v h_v + S_h \rho_h h_h$, and a source term Q_a that accounts for the energy added or subtracted by a fluid source or sink.

As a result of this operator splitting, rock and fluid will heat or cool at different rates. However, for the spatial and time scales of the processes considered in this model, rock and fluid in a control volume can be assumed to be in thermal equilibrium at all times. The total energy of rock and fluid calculated as

$$H_t = \left(1-\phi\right) H_r + \phi H_f \tag{8}$$

will therefore be redistributed at every modeling time-step to ensure that fluid and rock have the same temperature.

Thermal equilibration of fluid and rock results in the current temperature of the respective control volume and the thermodynamic model provides the resultant thermodynamic phase relation as

$$H_t = \left(1-\phi\right) \rho_r h_r + \varepsilon\phi \left(S_l \rho_l h_l + S_v \rho_v h_v + S_h \rho_h h_h \right) \tag{9}$$

and introduces a discrepancy ε between the thermodynamic density ρ_f of the fluid mixture and the actual mass per pore volume ρ_m as

$$\varepsilon = \frac{\dfrac{m_l + m_v + m_h}{\phi V}}{S_l \rho_l + S_v \rho_v + S_h \rho_h} = \frac{\rho_m}{\rho_f} , \tag{10}$$

with the mass m and the control volume V.

To ensure strict mass conservation during calculations with operator splitting, we insert the term ρ_m into the equation of mass conservation (Eqn 2) and obtain the equation for advective mass transport

$$\frac{\partial \left(\phi \rho_m \right)}{\partial t} = -\nabla \cdot \left(v_l \rho_l \right) - \nabla \cdot \left(v_v \rho_v \right) + Q_{H_2O+NaCl} . \tag{11}$$

Likewise, the total mass of salt normalized per pore volume is related to its thermodynamic equivalent determined from the phase states at the respective TPX condition as

$$\frac{m_{NaCl}}{\phi V} = \varepsilon \rho_f X_f = \varepsilon \left(S_l \rho_l X_l + S_v \rho_v X_v + S_h \rho_h X_h \right) . \tag{12}$$

The bulk mass fraction is identical in the two expressions and is given by

$$X_f = \frac{m_{NaCl}}{m_{H_2O} + m_{NaCl}} = \frac{m_{NaCl}}{\rho_m \phi V}. \tag{13}$$

The equation for solute transport after operator splitting therefore reads

$$\frac{\partial\left(\frac{m_{NaCl}}{V}\right)}{\partial t} = -\nabla\cdot\left(v_l \rho_l X_l\right) - \nabla\cdot\left(v_v \rho_v X_v\right) + Q_{NaCl} \ . \tag{14}$$

The term ε arises because fluid pressure is kept constant during the thermal equilibration step and can be of critical importance whenever fluids cross phase boundaries. If the control volume equilibrated as a closed system, pressure could be varied until $\varepsilon = 1$ by expanding or compressing the fluid. However, in an interconnected domain, local variations in fluid pressure will also cause changes in the far-field pressure. By changing the velocity field, pressure diffusion will also influence advection between neighboring control volumes. Such a volume discrepancy is common for compositional models (Trangenstein and Bell 1989; Geiger et al. 2009; Fritz et al. 2012). The numerical scheme has to ensure that ε remains reasonably close to 1 throughout the simulation by introducing a correction term in the calculation of the pressure field during the subsequent time step.

2.5. Pressure Evolution and Velocity Field

For multi-phase flow of compressible fluids, a transient pressure equation can be derived from the mass conservation equation (Eqn 2) by expanding the derivative of ρ_f into its pressure component (Geiger et al. 2006a):

$$\frac{\partial\left(\phi\rho_f\right)}{\partial t} = \phi\frac{\partial\rho_f}{\partial t} + \rho_f\frac{\partial\phi}{\partial t} = \phi\left(\rho_f\beta_f\frac{\partial p}{\partial t} + \left(\frac{\partial\rho_f}{\partial t}\right)_p\right) + \left(1-\phi\right)\rho_f\beta_r\frac{\partial p}{\partial t}, \tag{15}$$

with the isenthalpic compressibility of the fluid β_f as defined in Equation 5 and the compressibility of the rock β_r. The density change at constant pressure and changing temperature and salinity can be calculated directly from the phase relations and fluid properties after the thermal equilibration and will be considered with the source term

$$\phi\left(\frac{\partial\rho_f}{\partial t}\right)_p = \phi\frac{\varepsilon\rho_f - \rho_f}{\partial t} = \phi\frac{\rho_m - \rho_f}{\partial t} = Q_p. \tag{16}$$

Inserting the density derivative (Eqn 15), the phase velocities (Eqn 1) and the pressure source term (Eqn 16) into the mass conservation equation (Eqn 2) gives the equation for transient fluid pressure:

$$\begin{aligned}\rho_f\left[\phi\beta_f + \left(1-\phi\right)\beta_r\right]\frac{\partial p}{\partial t} = \nabla\cdot\left[k\left(\frac{k_{rl}\rho_l}{\mu_l} + \frac{k_{rv}\rho_v}{\mu_v}\right)\nabla p\right] \\ -k\left(\frac{k_{rl}\rho_l^2}{\mu_l} + \frac{k_{rv}\rho_v^2}{\mu_v}\right)g + Q_{H_2O+NaCl} + Q_p\end{aligned} \ . \tag{17}$$

This equation has a diffusion-type formulation even though it is derived from an equation describing an advective process.

2.6. Control Volume Finite Element Method

The governing equations are solved using the finite element and control volume capabilities of the CSMP++ simulation tool (Matthai et al. 2007), with the geometric relationships and naming conventions described in Figure 2. The Control Volume Finite Element Method (CVFEM) seeks to combine the advantages of the Control Volume Method (CVM) and the Finite Element Method (FEM) and to mitigate their limitations, by using the geometric flexibility of the FEM and the ability of the CVM to reproduce strong gradients (Forsyth 1991; Voller 2009). The general CVFEM formulation of a steady-state advection-diffusion-type equation solving for a property ψ is

$$\sum_{j=1}^{f} \int_{A_j} \kappa \nabla \psi \cdot \vec{n} dA - \sum_{j=1}^{f} \int_{A_j} \left(\vec{v} \cdot \vec{n} \right) \psi \, dA = 0 , \tag{18}$$

where the first term describes diffusive processes and the second term advective processes, f specifies the number of facets within all elements in support of the respective control volume (blue line in Figure 2A), A_j denotes the area of the respective facet, κ represents a diffusivity term and $\vec{v} \cdot \vec{n}$ is the velocity projected to the facet normal (Voller 2009).

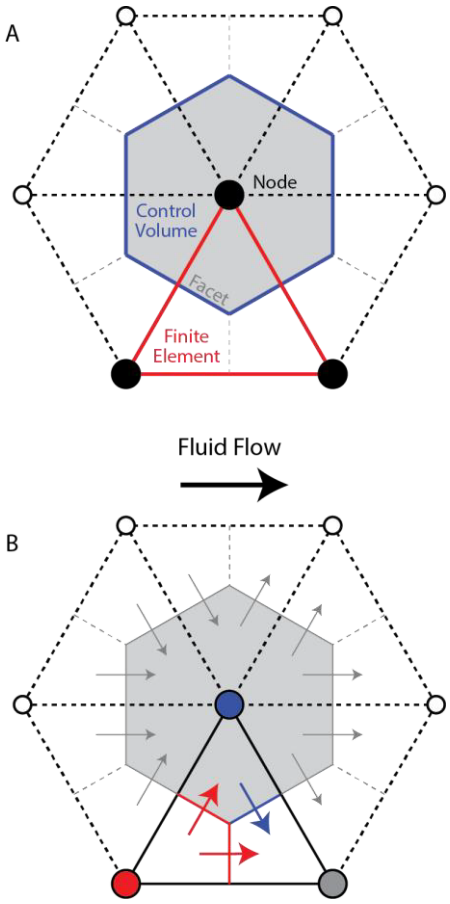

Figure 2. Construction of finite element and control volume capabilities. (**A**) The user-defined finite element mesh (red) is superimposed by a node-centered control volume mesh (blue) by the CSMP++ model. Facets are constructed from the mid-side point of the element's faces to the element's barycenter and define the segments of the control volume. (**B**) Fluid flow is calculated across these facets by projection onto the facet normal, exemplified by the red, blue, and gray

arrows representing horizontal flow from left to right (black arrow) and the colors indicating the upwind nodes within the finite element.

Given its diffusion-type character, we can formulate our pressure equation (Eqn 17) according to the first term of the general CVFEM formulation

$$\sum_{j=1}^{f} \int_{A_j} \kappa \nabla \psi \cdot \vec{n} dA = 0 \,, \tag{19}$$

resulting in

$$\begin{aligned} c_m \frac{d}{dt} \int_V p dV = & \sum_{j=1}^{f} \int_{A_j} c_{sl} \nabla p \cdot \vec{n} dA + \sum_{j=1}^{f} \int_{A_j} c_{sv} \nabla p \cdot \vec{n} dA \\ & - \sum_{j=1}^{f} \int_{A_j} \vec{G}_l \cdot \vec{n} dA - \sum_{j=1}^{f} \int_{A_j} \vec{G}_v \cdot \vec{n} dA \\ & + \int_V Q_{H_2O+NaCl} dV + \int_V Q_p dV \end{aligned} \,, \tag{20}$$

with the coefficient of the mass matrix

$$c_m = \rho_f \left[\phi \beta_f + (1-\phi) \beta_r \right], \tag{21}$$

the coefficients of the stiffness matrix

$$c_{si} = k \frac{k_{ri} \rho_i}{\mu_i} \,, \tag{22}$$

and the gravity components

$$\vec{G}_i = k \frac{k_{ri} \rho_i^2}{\mu_i} g \nabla z \tag{23}$$

for the mobile phases $i = \{l, v\}$.

With this formulation, the general diffusivity term κ of Equation (19) is replaced by the hydraulic conductivity as defined by c_{sl} and c_{sv}. However, averaging diffusion constants to the facet's midpoint as normally done in the diffusion term within the FEM requires interpolation or averaging of nodal fluid properties, which is difficult at phase transitions and may result in unrealistic thermodynamic values.

In a finite element-finite volume (FEFV) scheme (Geiger et al. 2004; Coumou 2008), which was the precursor of the numerical scheme presented here, c_{sl} and c_{sv} were calculated as elemental variables by taking into account the upwind direction within the element. However, this approach still required averaging of fluid properties. In the presence of strong gradients in fluid properties, phase transitions within an element, or large source terms $Q_{H_2O+NaCl}$ and Q_p, numerical solutions became unstable, because the pressure equation (Eqn 17) and mass advection (Eqn 11) can

considerably deviate from each other, despite being derived from the same equation of mass conservation (Eqn 2).

Mass advection calculated on the control volume mesh can be described by the second term of the general CVFEM formulation as

$$\sum_{j=1}^{f} \int_{A_j} \left(\vec{v} \cdot \vec{n}\right) \psi_u \, dA = 0 \,, \tag{24}$$

where the subscript u indicates that the fluid properties ψ are taken from the upstream node of the respective facet (Figure 2B). In order to prevent deviation between the calculations of fluid pressure and mass advection, we reformulate the pressure equation as a combination of the two terms of the CFVEM as given by Equations 17 and 24, and obtain:

$$\begin{aligned} c_m \frac{d}{dt} \int_V p dV = & \sum_{j=1}^{f} \int_{A_j} \left(k \nabla p \cdot \vec{n}\right) \left(\frac{k_{rl} \rho_l}{\mu_l} \right)_u dA + \sum_{j=1}^{f} \int_{A_j} \left(k \nabla p \cdot \vec{n}\right) \left(\frac{k_{rv} \rho_v}{\mu_v} \right)_u dA \\ & - \sum_{j=1}^{f} \int_{A_j} \left(k \cdot g \cdot \vec{n}\right) \left(\frac{k_{rl} \rho_l^2}{\mu_l} \right)_u dA - \sum_{j=1}^{f} \int_{A_j} \left(k \cdot g \cdot \vec{n}\right) \left(\frac{k_{rv} \rho_v^2}{\mu_v} \right)_u dA \,. \\ & + \int_V Q_{H_2O+NaCl} dV + \int_V Q_p dV \end{aligned} \tag{25}$$

By taking all fluid properties as upstream-weighted nodal variables when computing the coefficients of the stiffness matrix according to Equation 25, they represent the exact values of the fluids stored in the respective control volume as calculated from the thermodynamic model. Only the permeability k remains as an element property.

The coefficient of the mass matrix c_m (Eqn 21) also has to be calculated as a nodal property rather than being evaluated on the constraint points of the finite element. This way, the fluid compressibility can directly react to the pressure source terms $Q_{H_2O+NaCl}$ and Q_p which should also be formulated as nodal properties. This spatial discretization is essential because the compressibility β_f and, therefore, c_m vary over several orders of magnitude (Grant and Sorey 1979), so that averaging or interpolation will result in physically meaningless numbers at phase transitions.

The CVFEM formulation calculates a pressure gradient that is piecewise constant across an element. However, phase velocities are no longer defined on the element's barycenter because relative permeabilities k_{ri}, fluid viscosities μ_i and densities ρ_i will vary between the facets of the element. Consequently, when computing the advection of mass, solute and heat on the control volume mesh, only the pressure gradient is projected onto the facet and the fluid properties are taken from the same upwind node as in the formulation in the pressure equation. Now, the spatial and temporal discretizations of all the variables in the pressure equation (Eqn 17) are identical to the discretizations for advective mass transport (Eqn 11), which is consistent with the fact that they are both derived from the mass conservation equation (Eqn 2).

For graphical representations of the results, Darcy and pore velocities at the element's barycenter are calculated as a post-processing step using interpolated upstream-weighted fluid properties.

These velocities are not used for the transient flow calculations and should not be used for any further calculations that require rigorous mass and energy balances.

To ensure that the numerical solution of the pressure diffusion equation is stable and computationally efficient on the one hand, and minimize numerical dispersion so as to resolve sharp fronts during advection-dominated transport on the other hand, the pressure equation is integrated in time with a semi-implicit formulation while the advection equation is integrated in time with an explicit formulation. Solving the pressure diffusion equation semi-implicitly in time results in a set of linear differential equations that needs to be inverted at every time step. Since the resulting matrix is sparse, symmetric and positive definite, we do this in a computationally efficient manner using the algebraic multi-grid solver SAMG (Stüben 2001). The stronger coupling of the pressure equation to the calculation of advection terms keeps the discrepancy value ε close to 1, i.e. the mass stored in the pore volume is almost identical to the thermodynamic density throughout the simulation when computed in the right sequence and carefully acknowledging time-stepping restrictions imposed by the explicit time-discretization of the advection step.

2.7. Computational Sequence and Time Stepping

The governing equations are solved in a sequential approach (Figure 3). Fluid properties are kept at the current time level and only updated after all advective and diffusive processes have been computed. The sequencing attempts to capture the dynamics of the relevant physical processes with each process being solved using the numerical method that is best-suited for its governing equation. The sequential approach aims to provide a strong coupling of the system of equations so as to ensure that the solution is stable, consistent, and convergent.

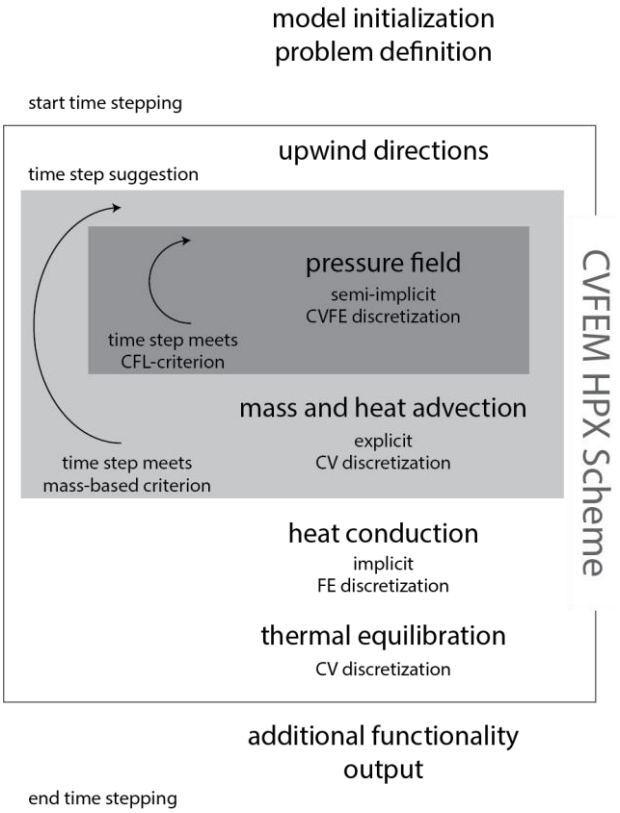

Figure 3. Computational sequence of the control volume finite element method (CVFEM) for flow of subsurface fluids characterized by enthalpy, pressure, and composition (HPX).

The pressure equation uses a semi-implicit discretization, where the equation is solved implicitly but the non-linear coefficients are taken from the previous time-step rather than estimated iteratively at the next time-step; properties are not evaluated or averaged at an intermediate time-level or estimated using a predictor-corrector scheme (e.g. Coumou 2008; Weis et al. 2008). In conjunction with the calculation of mass, heat and solute transport with explicit discretization in time, our implementation of the CVFEM can be regarded as a modification of the standard implicit pressure-explicit concentration approach IMPEC, which is a common procedure for integrating compositional models in time (Huber and Helmig 1999; Gerritsen and Durlofsky 2005). Heat conduction is solved using a fully implicit discretization in time because the relevant coefficients are assumed to be constant. The overall scheme thus includes a mixture of implicit, semi-implicit and explicit discretizations in time. However, the explicit integration of the advection equation imposes limits to the overall permissible size of the time steps.

After setting up the constants and the initial and boundary conditions, the transient calculations advance with variable time steps dt. During the temporal evolution of the simulated hydrothermal system, periods of fast fluxes of low-density fluids (e.g. vapor transport in a boiling zone) will require time-step sizes that are orders of magnitude smaller than those required during phases of single-phase convection of liquid-like fluids. As soon as the time-step criteria permit larger time steps (e.g. after a boiling event) the time-step size is gradually increased in order to avoid large variations in time-step size. At the beginning of any time step, dt is increased by a user-specified factor, e.g. 1.01 (increase by 1%) or 1.1 (increase by 10%), up to a user defined maximum time step.

This time step is used to solve the semi-implicit pressure equation (Eqn 17) (Figure 3). From the solution of the pressure equation, the pressure gradients in each finite element can be obtained using the derivatives of the finite-element basis functions. To determine the maximum permissible time step for the advection step computed with Equations 7, 11 and 14, the Courant-Friedrich-Levy (CFL) criterion is evaluated once the pressure gradients have been computed. The CFL is calculated for fluxes of both the liquid and vapor phase across every facet as

$$dt \leq \frac{\phi \, dx}{\vec{v} \cdot \vec{n}}, \tag{26}$$

with the distance dx between the nodes connected by the respective facet and the subscript i indicating the values of the respective phase at the upstream node u. If the suggested time step is larger than the smallest calculated CFL criterion, the pressure equation is solved again with an accordingly smaller time step. This is repeated until the time step fulfills the CFL criterion (inner loop in Figure 3).

As the upwind direction may switch after the new pressure field has been calculated, we experimented with iterative procedures that solve for a new pressure field using upwind nodes consistent with the new time level. However, we found that 1) all procedures were computationally expensive, 2) directions mainly switch at facets with very little flow, e.g. with orientations in the direction of flow, and 3) updating the upwind nodes had no visible effect on the results. To save computational time, we therefore use the old velocity field to define the upwind nodes for every facet, which is also consistent with using fluid properties from the same time step.

After advecting mass, heat and solute, the method performs a second mass-based time-step criterion check (outer loop in Figure 3). Here, the flux of mobile phases out of a control volume is balanced with the mass stored in the control volume in the respective phase i at the old time level as

$$dt \leq \frac{\phi \varepsilon S_i \rho_i}{\left[\sum_{j=1}^{f} \int_{A_j} \left(k \nabla p \cdot \vec{n} \right) \left(\frac{k_{ri} \rho_i}{\mu_i} \right)_u dA - \sum_{j=1}^{f} \int_{A_j} \left(k \cdot g \cdot \vec{n} \right) \left(\frac{k_{ri} \rho_i^2}{\mu_i} \right)_u dA \right]_{outflow}}. \quad (27)$$

If the outflow exceeds the content of mass, heat or solute available in a control volume, the time step will be reduced accordingly and the pressure equation will be recalculated with the new suggested time step. Both time-step criteria ensure that flow across an entire control volume cannot occur during one single time step in an explicit time discretization. This procedure proved to be essential to avoid occasional oscillations in the highly-compressible two-phase region.

After both time-step checks have passed successfully, heat conduction in the rock can be performed without any further time-step control as the heat conduction equation (Eqn 6) is solved with an implicit finite element Euler formulation using the Galerkin method (Geiger et al. 2004; Coumou 2008) (Figure 3). Since the energy contents of both rock and fluid have now changed, a thermal equilibration is performed at constant pressure, and fluid properties are updated for the new temperature (Figure 3). This will inevitably lead to a mismatch ε (Eqn 10) between the fluid mass stored in the pore space and the new thermodynamic density, especially when crossing phase boundaries, and result in the pressure source term Q_p (Eqn 16). The updated fluid properties and source terms are then used in the pressure equation of the following time step.

This new CVFEM-HPX scheme describes transient multi-phase flow of H_2O-NaCl fluids. Any additional functionality relevant for the system, such as temporal variations in rock properties, can be added after equilibration and before starting the new time step.

2.8. Rock Properties

The continuum approach assumes that permeability can be treated as a material property that is constant over a representative elementary volume. Depending on the nature and heterogeneity of the system, the model domain may require local mesh refinement in order to be able to represent important geological features with contrasting permeabilities such as fault zones that may act as fluid conduits.

In contrast to shallow groundwater systems at moderate temperatures where permeability is mostly assumed to be an intrinsic property of the rock, high-temperature hydrothermal systems in fractured rocks at deeper levels of the crust can have a dynamic permeability. In a continuum, porous medium approach, fluid-rock interactions can be incorporated by mapping constitutive relationships describing dynamic permeability for a respective finite element. A temperature-dependent permeability, for example, can describe the transition from brittle to ductile rock behavior (e.g. Hayba and Ingebritsen 1997; Fournier 1999; Driesner and Geiger 2007; Gruen et al. 2012; Weis et al. 2012) and a fluid pressure-dependent permeability can describe hydraulic fracturing and fault activation (e.g. Rice 1992; Rojstaczer et al. 2008; Taron et al. 2009; Lupi et al. 2011; Weis et al. 2012). Chemical fluid-rock interactions, such as serpentinization, quartz precipitation or more complex chemical reactions, can also lead to changes in porosity and

permeability and influence the hydrology (e.g. Taron et al. 2009; Iyer et al. 2010; Steele-Maclnnis et al. 2012).

Permeability is a tensor variable and can be highly anisotropic. Resolving anisotropic permeabilities with strong variations in the directional permeability remains a challenge for many numerical techniques that operate on structured grids. The finite difference method, as applied by HYDROTHERM, requires k-orthogonal grids; that is, the principal axes of the permeability tensor must be parallel to the lines connecting neighboring grid points in each spatial direction and, furthermore, the interfaces between two neighboring grid points are perpendicular to the lines connecting them. A lack of k-orthogonality can lead to numerical errors unless more complex numerical discretization schemes are employed such as multi-point flux approximations or mimetic finite difference methods (e.g. Aavatsmark 2002; Lie et al. 2012). Although the integrated finite difference approach, as applied by TOUGH2, gives more flexibility to resolve complex geological structures, the requirement of k-orthogonality still remains and generating IFD meshes that are k-orthogonal is not straightforward.

The CVFEM method has restrictions as well. A Delaunay triangulation is needed to ascertain physically correct upwind weighting of the flux terms (Forsyth 1991). However, modern finite element meshing algorithms almost always produce Delaunay grids (Shewchuk 2002). If anisotropy in the permeability tensor is strong, cases can be constructed where the flow field is calculated incorrectly with the CVFEM approach because of the lack of flux continuity in a single control volume (Edwards 2006). While finite volume discretization schemes exist that can deal with strongly anisotropic permeabilities on unstructured grids, these approaches pose other challenges when simulating multi-phase flow processes (Schmid et al. 2013).

The numerical method presented here has already been used to model the flow of phase-separating magmatic fluids in highly heterogeneous and transiently evolving permeability fields (Weis et al. 2012; Weis and Driesner 2013). However, heterogeneity and anisotropy of material properties is beyond the scope of the present study which focuses on the dynamics of multi-phase flow of H_2O-NaCl fluids. We hence keep rock properties constant and uniform, using an isotropic permeability of $k = 10^{-15} m^2$, a porosity of $\phi = 0.1$, a heat capacity of $c_{pr} = 880 \frac{J}{kg\,°C}$, a thermal conductivity of $K = 2 \frac{W}{m\,°C}$ and a rock density of $\rho_r = 2700 \frac{kg}{m^3}$ for all simulations presented below.

2.9. Simulating Magmatic-Hydrothermal Systems

As the model simulates transient flow of H_2O-NaCl fluids only, magmatic activity as a driving force for the hydrothermal system has to be parameterized or pre-assigned in the modeling domain. The current scheme offers three ways to do so that are common in the literature and can also be used in combination:

Defining a temperature anomaly representing a magmatic heat source (condition 1).

The initial outline of a magmatic intrusion within the modeling domain can be locally assigned as an anomaly with magmatic temperatures as initial conditions. This condition has been applied to investigate volcanic and geothermal systems (e.g. Cathles 1977; Norton and Knight 1977; Hayba and Ingebritsen 1997) and has the advantage that the extent of the magma chamber can be directly applied as a constraint. This method mimics a single emplacement of magma. Any further magmatic activity would overwrite parts of the modeling domain. Defining a constant temperature boundary condition can represent a continuous magmatic heat source outside the

modeling domain. This condition is usually applied to the bottom boundary of the domain and is common for simulations of mid-ocean ridge hydrothermal systems (e.g. Fontaine et al. 2001). This method has the advantage that the observed temperatures can be directly assigned to the system.

Defining a heat flux representing a subjacent magma chamber (condition 2).

This condition is also common for simulations of mid-ocean ridge hydrothermal systems (e.g. Coumou et al. 2008b; Coumou et al. 2009). By changing the source term Q_c accordingly, this condition has the advantage that the heat input can be directly controlled.

Defining a magmatic fluid source representing the fluid supply rate from a subjacent magma chamber (condition 3).

This condition is commonly applied for hydrous magma chambers releasing volatiles during crystallization (e.g. Hanson 1995; Gruen et al. 2012; Weis et al. 2012). In our transport scheme, fluids are characterized by their mass, enthalpy, and salt content, and magmatic volatiles can enter the system with the source terms $Q_{H_2O+NaCl}$, Q_{NaCl} and Q_a.

All three conditions will be used in simple forms as benchmarking examples. We used version 3.1 of HYDROTHERM, a simulation tool developed and maintained by the US Geological Survey, which can be downloaded from the internet for free, and the PetraSim version of TOUGH2, which can be licensed. Both programs have graphical user interfaces, which provides comparatively easy access to perform simulations but also places a number of constraints on possible model configurations.

3. Results

We performed a series of one-dimensional (1D) advection-dominated examples with constant temperature conditions (condition 1) with and without salt, two-dimensional (2D) convection examples with constant heat flux (condition 2), and 2D fluid expulsion examples with a constant source of magmatic fluids of varying enthalpies and salinities (condition 3).

3.1. One-dimensional simulations

All 1D benchmarks are performed with constant temperature and fluid pressure conditions on both ends of a domain of 2 km length with a mesh resolution of Δx = 10 m. Initially, the domain has a linear pressure gradient given by the values at the end points while the temperature is constant and equal to the temperature at the downstream end. The domain is first oriented horizontally with higher pressure and temperature values at the left boundary node (no gravitational effects, hot fluids flow from left to right), and then rotated to the vertical with the higher values at the bottom (with gravitational effects). The assigned pressure gradient exceeds the hydrostatic pressure gradient imposed by the colder fluids from the initial conditions, so that the hotter fluids move upward in the vertical simulations.

For comparison, HYDROTHERM simulations have been set up with the same settings. For the horizontal benchmarks, the mesh is a pseudo-2D domain where the grid spacing is Δx = 10 m in the horizontal direction and the model is only one single cell high (Δy = 10 m) in the vertical direction. The vertical examples use a similar mesh, with a grid spacing of Δy = 10 m and one single cell in the horizontal direction with a width of Δx = 10 m. Since HYDROTHERM applies boundary conditions on the nodes at the center of the elements, the domain is represented by a length of 2010 m and 201 elements. HYDROTHERM also uses a different numerical technique to solve the equations, applying a fully-coupled, fully-implicit and hence iterative scheme. This method allows

for larger time steps as it is not tied to the CFL-criterion. These larger time steps, however, can cause numerical dispersion which leads to a "smearing" of the thermal front. The time-step size cannot be controlled directly in the interactive version of HYDROTHERM. However, by setting the output interval of the variables to one year and setting the maximum time-step size in our CSMP++ simulations to the same value, we were able to enforce comparable time steps for both models.

3.1.1. Pure water, single-phase flow

We performed six examples of 1D flow on a heating path (Figure 4). The first example shows horizontal flow of a 350°C fluid into an initially 150°C domain (Figure 4A). As fluid pressure is fixed by the 50 and 25 MPa boundaries, the fluids stay in the single-phase liquid (or liquid-like) field. The thermal front has progressed approximately to the middle of the domain after 250 years of simulation time. Results from HYDROTHERM and CSMP++ are almost identical. Rotating the domain to the vertical also shows an excellent match (Figure 4B). Here, the thermal front progresses about three times slower due to gravitational effects and reaches the middle after about 750 years.

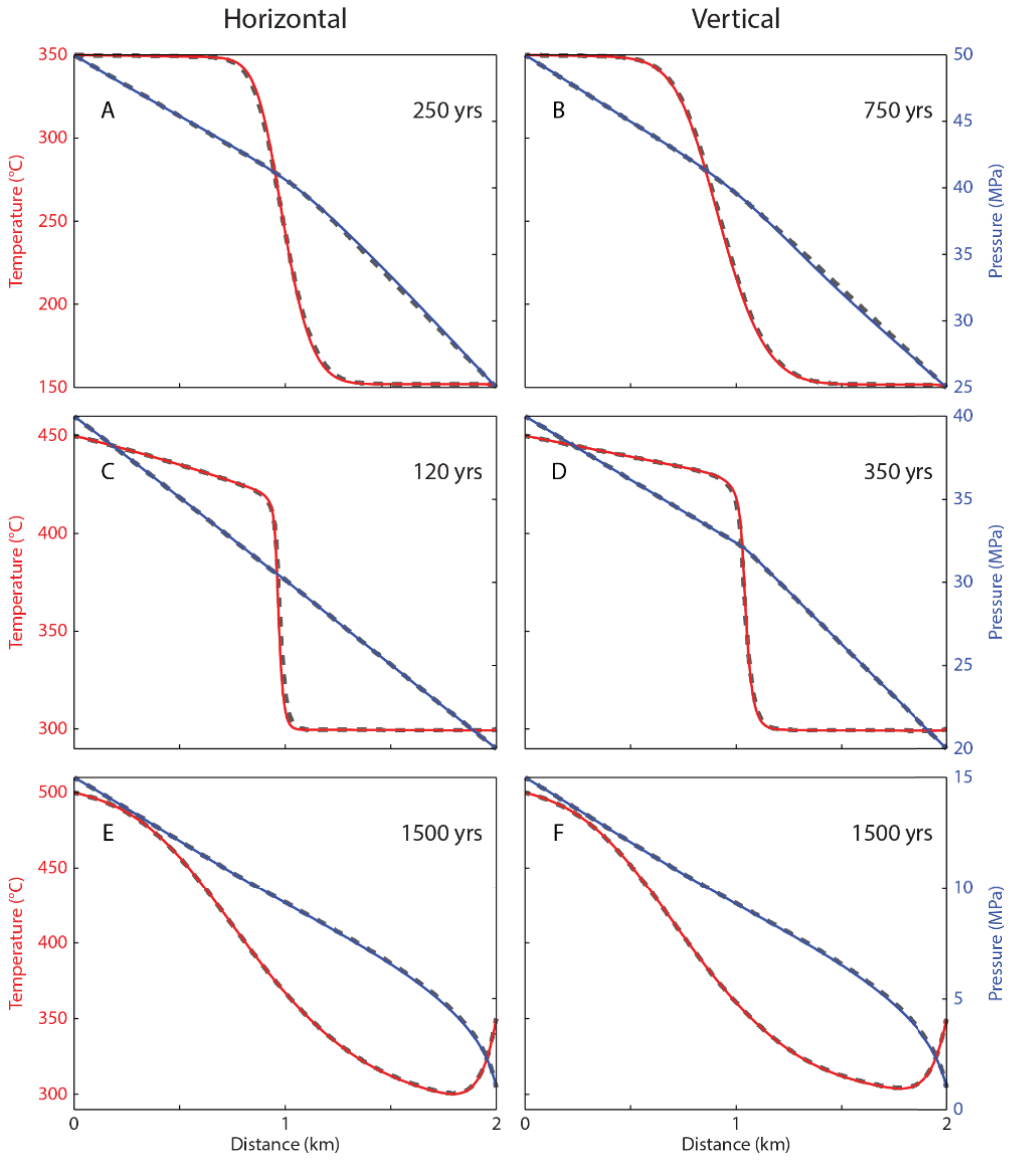

Figure 4. Snapshots of single-phase, one-dimensional simulations of a heating thermal front in horizontal (**A,C,E**) and vertical (**B,D,F**) orientation. Results for fluid pressure (blue) and temperature (red) from CSMP++ are plotted as solid lines, results from HYDROTHERM as dashed lines (dark gray).

Increasing boundary temperatures to 450°C and 300°C and lowering fluid pressure to 40 MPa and 20 MPa, respectively, moves the fluids into the so-called supercritical field right above the critical point of pure water (374°C, 21.1 MPa). The thermal front in these two examples has passed through the domain about halfway after 120 years for the horizontal case (Figure 4C) and after 350 years for the vertical case (Figure 4D). Again, the agreement of results obtained with CSMP++ and HYDROTHERM is nearly perfect.

With a further increase in temperature (500°C and 350°C) and further decrease in pressure (15 MPa and 1MPa), the fluids enter the single-phase vapor field. This example develops no clear thermal front since temperatures at the right side of the domain drop drastically by up to 50°C (Figure 4E-F). This effect results from the increase in fluid pressure, which causes a vapor of constant enthalpy to cool to lower temperatures. Due to the low density, the gravity component has a minor effect only and the propagation of the thermal front after 1500 years looks very similar for both the horizontal and vertical case. Again, there is excellent agreement for the results obtained with CSMP++ and HYDROTHERM.

3.1.2. Pure water, two-phase flow

We computed a further one-dimensional simulation where we inject 400°C hot steam into a 150°C liquid-dominated domain (Figure 5). Fluid pressure is kept below the critical point of H_2O with fixed values of 20 MPa and 1 MPa at the boundaries, resulting in two-phase flow conditions during the advance of the hot steam. This two-phase field is bounded by two distinct thermal fronts: in the horizontal case the main front has progressed about 1000 m after 200 years while the second front has progressed about 750 m into the domain (Figure 5A). In between these fronts, the thermal profile follows the boiling curve. In the vertical case the main front has progressed about halfway after 1000 years (Figure 5C) and the two-phase region is about twice as wide as in the horizontal case.

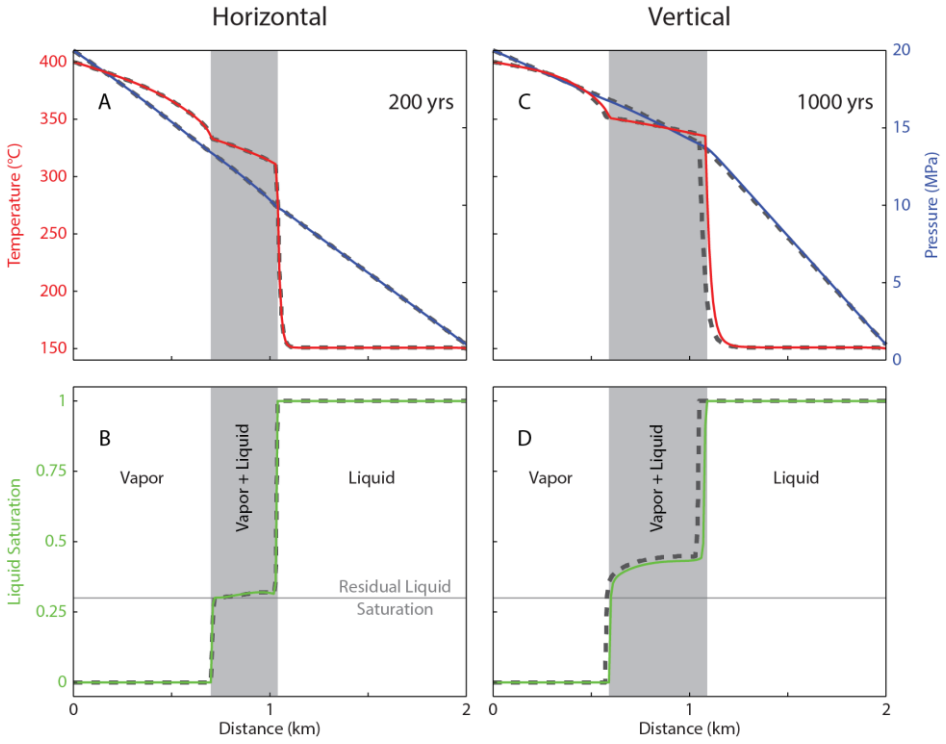

Figure 5. Snapshots of two-phase, one-dimensional simulations with pure water in horizontal (**A,B**) and vertical (**C,D**) orientation. Results for fluid pressure (blue), temperature (red) (A,C), and liquid saturation (green) (B,D) from CSMP++ are plotted as solid lines, results from HYDROTHERM as dashed lines (dark gray).

In the horizontal case the volumetric saturation of the liquid phase settles at a value of 0.3 in the boiling zone (Figure 5B). This value was chosen as the residual saturation of the liquid phase, i.e. the saturation at which the relative permeability of the liquid phase is zero and the residual liquid becomes immobile. In the vertical case the liquid saturation stays above that value (Figure 5D). Here, the results with CSMP++ show a slight lead of the thermal front as compared to the results with HYDROTHERM, while the results of the horizontal case match perfectly.

In a modification of this example, we assign a smaller pressure gradient by lowering fluid pressure at the left end of the domain to 4 MPa (Figure 6A-B). This example can only be performed in a horizontal orientation, as the pressure gradient assigned by the boundary conditions is smaller than the hydrostatic pressure gradient of the initial 150°C fluid in the vertical case. Also lowering temperature at that boundary to 300°C allows for an additional comparison with results from TOUGH2 as the conditions are now within the model's temperature range. For TOUGH2, a horizontal pseudo-3D domain in the PetraSim software has been configured similarly to HYDROTHERM with a total length of 2010 m. The results show an excellent match of all three models (Figures 6A-B).

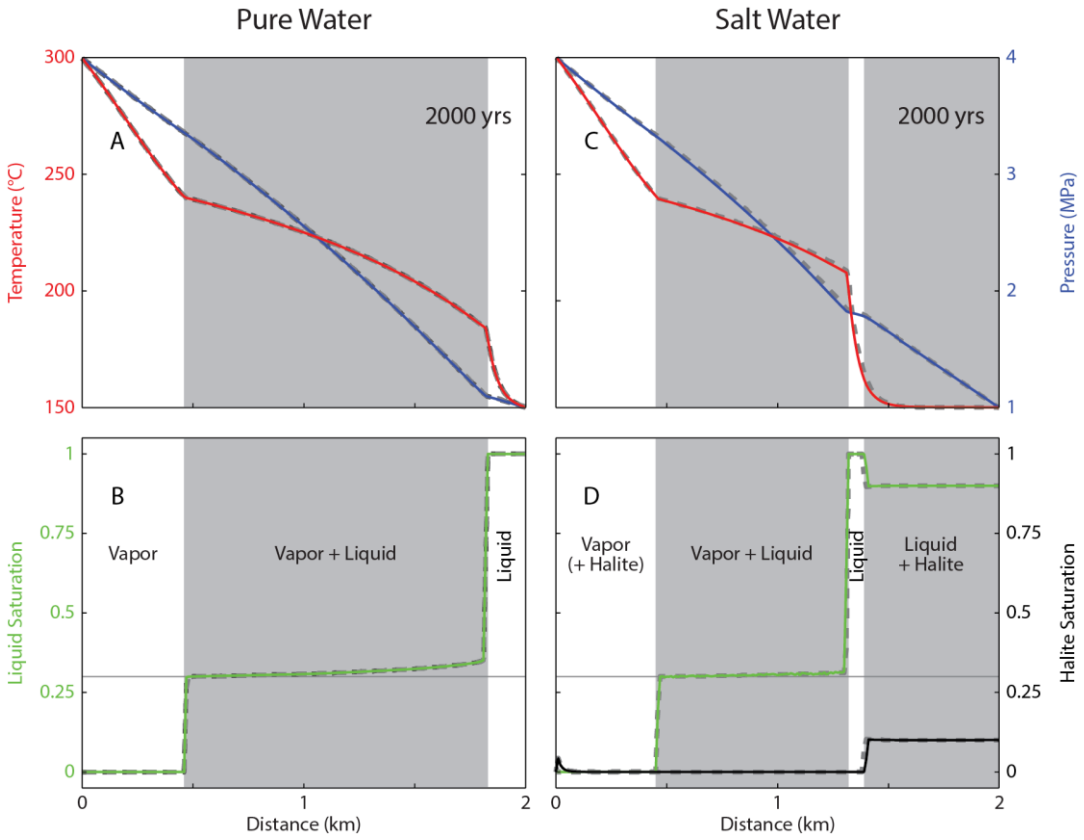

Figure 6. Snapshots of multiphase, one-dimensional simulations with (C,D) and without (A,B) salt. Results for fluid pressure (blue), temperature (red) (A,C), liquid saturation (green), and halite saturation (black) (B,D) from CSMP++ are plotted as solid lines, results from HYDROTHERM (pure water only; dark gray) and TOUGH2 (gray) as dashed lines.

3.1.3. Salt water, multi-phase flow

We continue the comparison with TOUGH2 and add salt to the fluid in the simulations. We keep the pressure-temperature conditions as in the last example (300°C, 4 MPa at the left and 150°C , 1 MPa at the right boundary) and initialize the liquid in the domain as salt saturated, with an initial halite saturation of 0.1. The node at the left boundary is kept as pure water vapor (Figure 6C-D).

The PetraSim version of TOUGH2 uses a different permeability-dependence on halite saturation than we normally use with CSMP++ (see section 2.1). For this particular benchmarking example we therefore adjusted the relative permeability functions to still be linear, albeit without consideration of the effect of solid halite. Instead, halite reduces permeability as

$$k = k_0 \left(1 - S_h\right)^2, \tag{28}$$

with the initial permeability k_0.

The hot steam at the left boundary progressively heats the domain and dissolves the immobile solid halite phase (Figure 6D), moving fluids from the liquid-halite field to a single-phase liquid field. Boiling starts shortly afterwards, moving the fluids into the two-phase vapor-liquid field. The residual liquid saturation has been kept at a value of 0.3, where the liquid saturation remains in the vapor-liquid field as in the horizontal simulations with pure water. After a brief transition through the three-phase coexistence of vapor, liquid and halite, the heated part of the domain lies in the vapor-halite field. However, halite saturations in this region are close to zero, since most NaCl has already been washed out through the right side of the domain. Again, results from CSMP++ and TOUGH2 are in very good agreement.

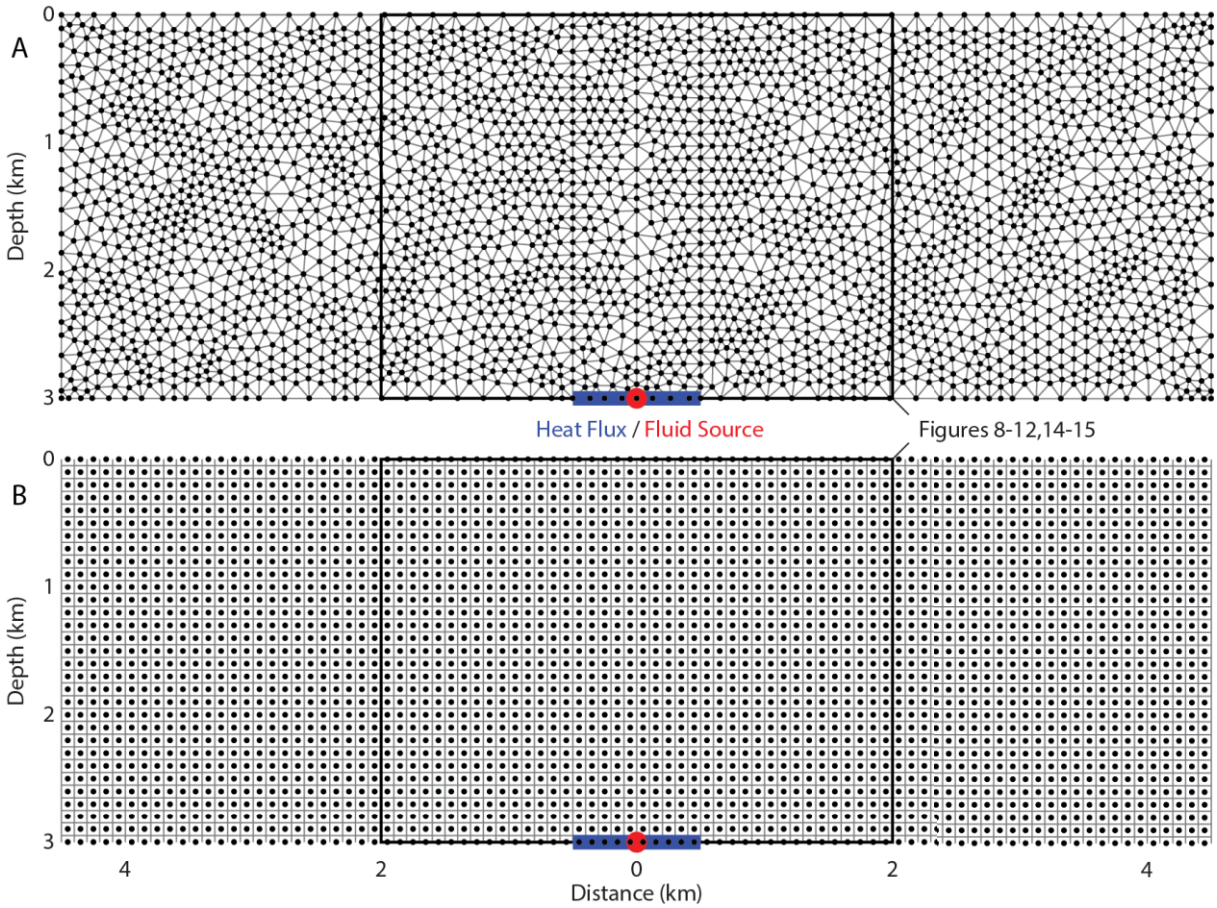

Figure 7. Mesh and model configuration for two-dimensional simulations. (**A**) CSMP++ uses an unstructured grid with about 2600 nodes representing a mesh of about 5000 triangular elements. (**B**) The mesh in HYDROTHERM and TOUGH2 has been set to a uniform grid with a spatial resolution of 100 m, leading to a total number of 2790 elements. We ensured that the distance from the nodes at the bottom to the nodes at the top is exactly 3 km by assigning a domain height of 3100 m in the graphical user interface. We also used coarser and finer meshes (not shown) to investigate the influence of spatial resolution on the results. The blue lines indicate the location for the increased heat flux (condition 2), and the red points mark the injection location of the magmatic fluid source (condition 3).

3.2. Two-dimensional simulations

The 2D examples are performed on a rectangular domain of 9 km width and 3 km depth (Figure 7), representing a vertical section through the upper crust. The top boundary represents the Earth's surface and is kept at atmospheric pressure and a temperature of 10°C. At the bottom, a constant background heat flux of $Q_c = 0.05 \frac{W}{m^2}$ is applied. In all simulations, the domain has been initialized with a constant temperature of 10°C and a hydrostatic pressure gradient. In the center, somewhere below the bottom boundary of the domain, we assume a magmatic source which we represent either as a heat source, by locally increasing the heat flux along a 1 km wide segment located in the center of the bottom boundary (condition 2), or as a fluid source of magmatic volatiles (condition 3).

3.2.1. Pure water, single-phase flow

In a first 2D-simulation, an increased heat flux of $Q_c = 5 \frac{W}{m^2}$ was applied along a length of 1 km at the central part of the bottom boundary (Figure 7), which equals a total energy input of 5 kW considering a unit thickness of 1 m for the 2D modeling domain. A hydrothermal plume evolves with time, reaching temperatures greater than 300°C in the deeper center parts of the plume (Figure 8A-C). At quasi-steady state (Figure 8C), fluid pressures are lower in the center part due to lower densities of the heated fluids compared to the recharging, colder fluids at the sides. Fluid pressures and temperatures calculated by CSMP++ and HYDROTHERM show a very good match.

For the next example, instead of an increased heat flux, we inject hot fluids at the center node of the bottom boundary (i.e., at x = 4.5 km) as a fixed point source with a constant source rate of . We start with a moderate enthalpy fluid of , which results in a source term in the energy equation of = 20 kW (Fig. 8D–F). The addition of these hot fluids to the domain leads to a quasi-radial increase in fluid pressures accompanying propagation of the thermal front. This pressure anomaly relaxes with the breakthrough of the injected fluids to the surface, due to their lower viscosity and the reduced gravitational load of the lower density fluids (Fig. 8F).

Again, fluid pressures and temperatures calculated by CSMP++ and HYDROTHERM agree very well. The rising plume in the HYDROTHERM simulation tends toward a more triangular or pointed progression, while the plume in the CSMP++-simulation progresses as a rounded, more radially oriented front.

We performed the same example with a coarser mesh resolution and with an increased mesh resolution in a central zone of 1 km width (Figure 9). The grid spacing in the HYDROTHERM meshes was varied in the horizontal direction and kept constant in the vertical direction to investigate the influence of aspect ratios of the structured grid. The results show that the spatial resolution has no significant influence on the results.

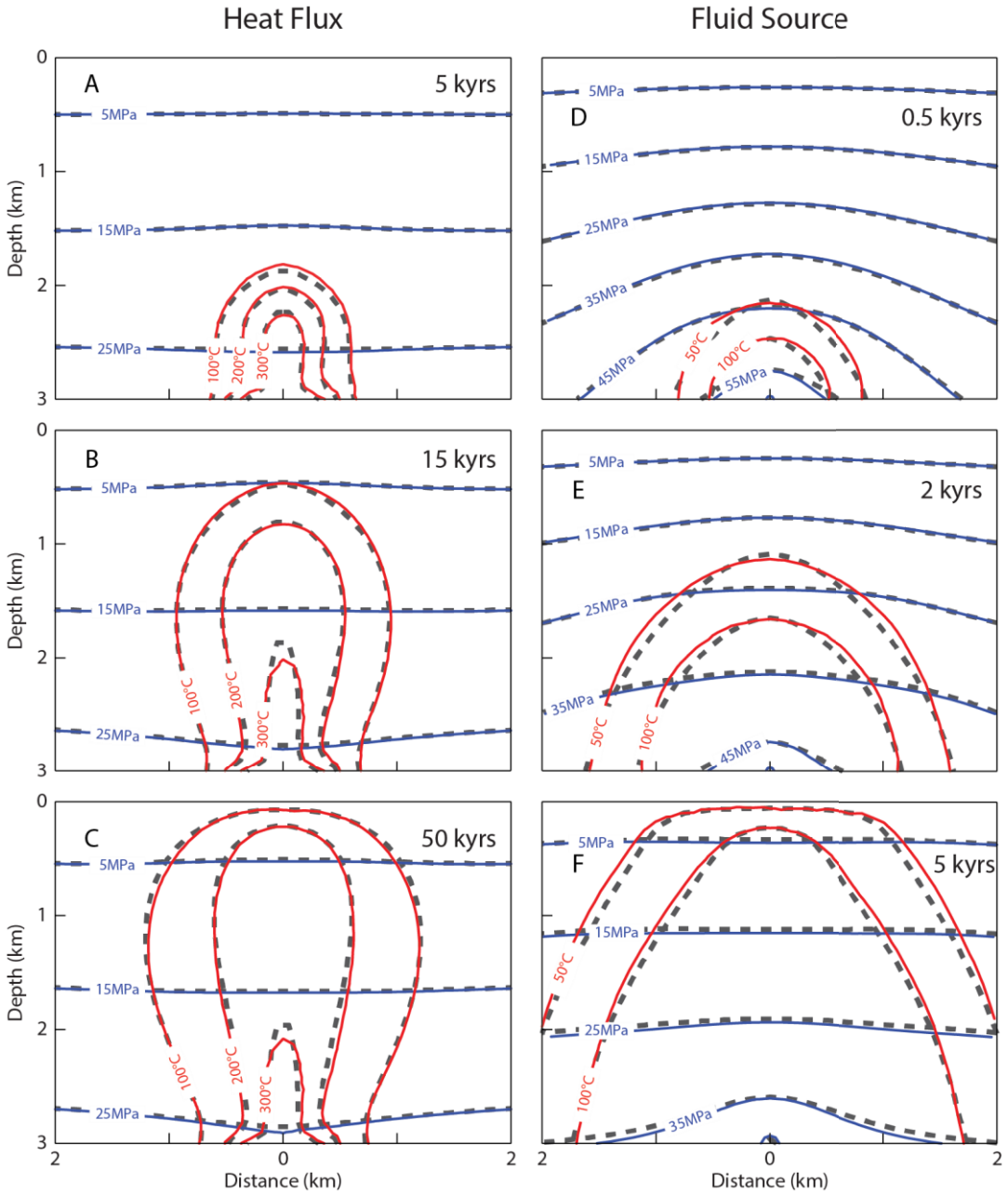

Figure 8. Snapshots of single-phase, two-dimensional simulations with an increased bottom heat flux (**A–C**) and a hot fluid source (**D–F**). Results for fluid pressure (blue) and temperature (red) from CSMP++ are plotted as solid lines, results from HYDROTHERM as dashed lines (dark gray). The excerpts show the center 4 km of the modeling domain of 9 km width (Fig. 7).

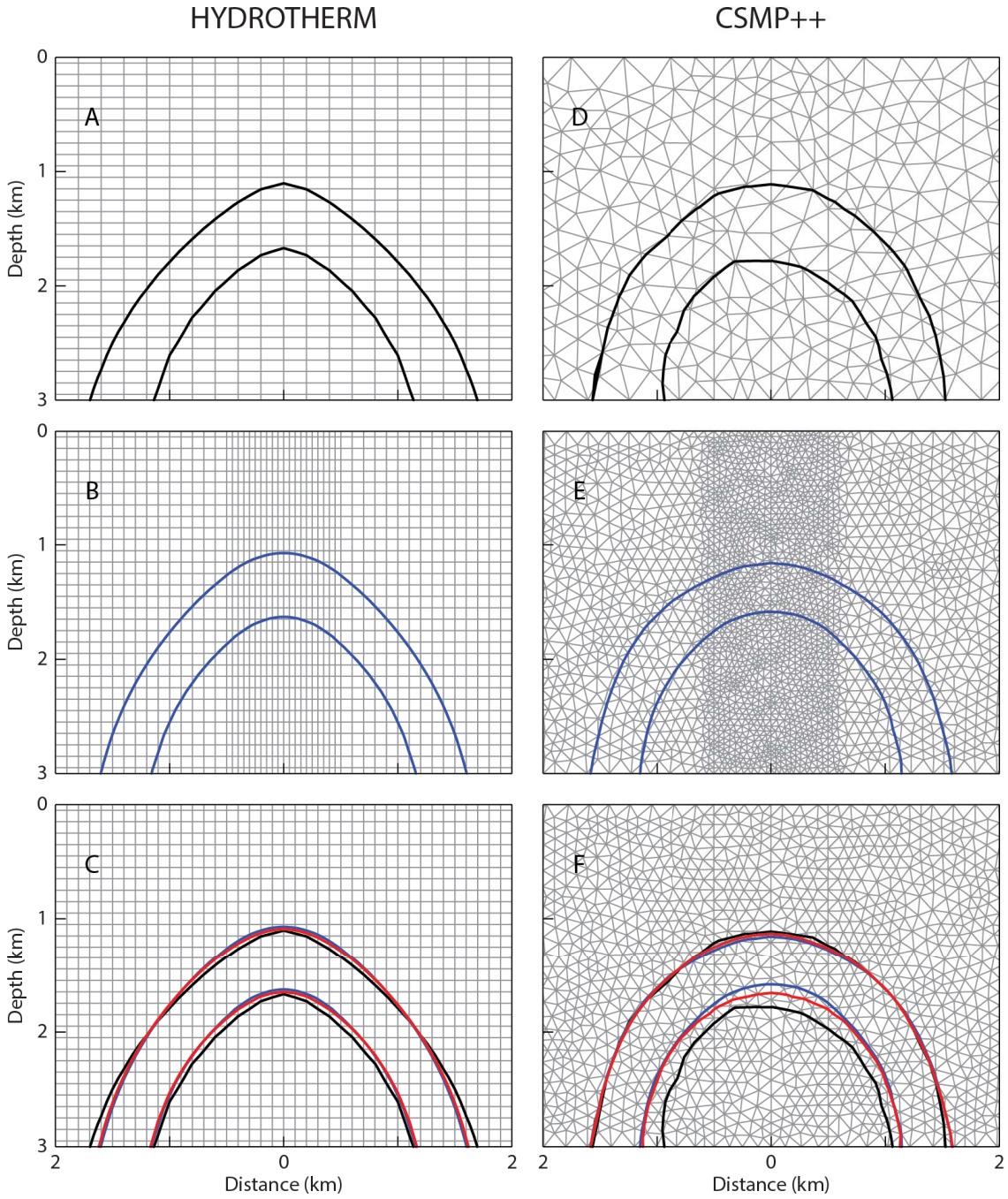

Figure 9. Mesh sensitivity of two-dimensional pure water simulations with fluid source (Fig. 8E). The plots show the 50°C and 100°C isotherms after 2000 years of simulation time. The bottom panels (**C, F**) show the results from the standard meshes used in this study (Fig. 7) as red lines with the results from the coarser meshes (**A, D**) as black lines and from meshes with a finer central part (**B, E**) as blue lines.

3.2.2. Pure water, two-phase flow

In order to produce hotter plumes that enter the two-phase field upon ascent, we increased the heat flux anomaly to $Q_c = 9 \frac{W}{m^2}$ (total energy input: 9 kW) and the enthalpy of the injected fluid to $h_f = 1.5 \frac{MJ}{kg}$ while keeping the source rate at $Q_{H_2O} = 0.04 \frac{kg}{s}$ which results in a source term in the energy equation of Q_a = 60 kW (Figure 10). The results for pressure, temperature and phase saturations for the quasi-steady state situation still match reasonably well, yet not as perfectly as in the 1D- and the single-phase 2D-simulations. Again, CSMP++ produces a slightly stronger outward propagation than HYDROTHERM. We also simulated the high-enthalpy source set-up

with TOUGH2 and the results agree very well with the ones from CSMP++ and HYDROTHERM (Figure 10B). HYDROTHERM and TOUGH2 produce nearly identical results.

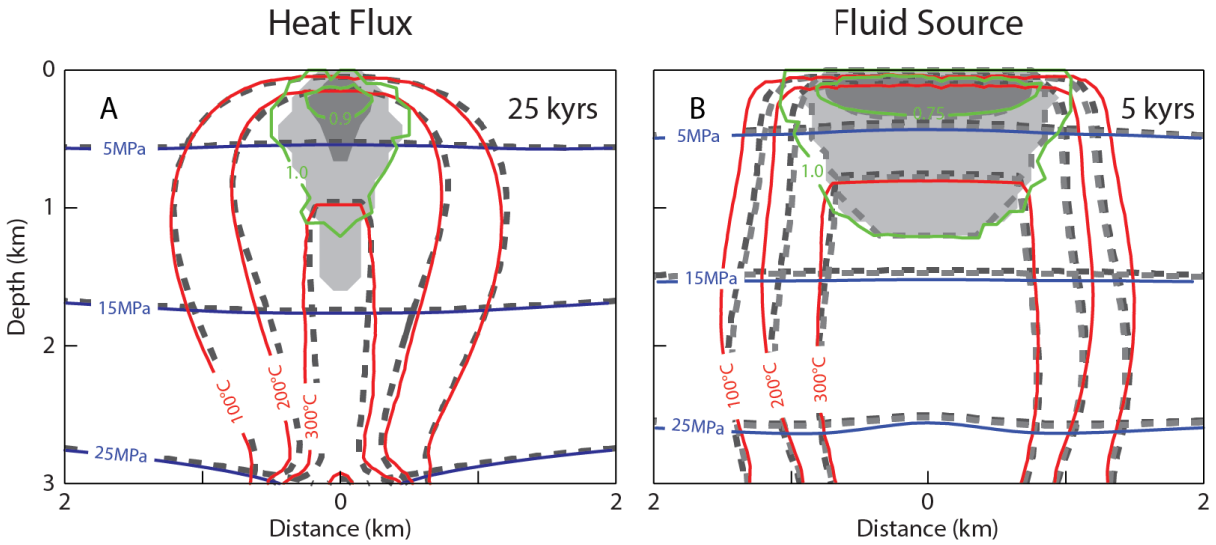

Figure 10. Snapshots of two-phase, two-dimensional simulations with increased heat input. Results for fluid pressure (blue), temperature (red), and liquid saturation (green) from CSMP++ are plotted as solid lines, results from HYDROTHERM as dashed lines (dark gray). The outer solid green line marks a liquid saturation of 1.0, indicating the extent of the two-phase field. The inner green line shows liquid saturation of 0.9 for the heat flux simulation (**A**) and 0.75 for the fluid source simulation (**B**). The gray-shaded areas show the same saturations as calculated by HYDROTHERM. Results from the fluid source simulation (B) with TOUGH2 are plotted as gray dashed lines.

Increasing the enthalpy of the input fluid leads to a stronger mesh and resolution dependence of the results (Figure 11). The tendency of the results from HYDROTHERM to develop triangular, pointed thermal fronts in comparison to a more radial progression with CSMP++ is enhanced compared to the results with lower enthalpy fluid (Figure 9). Changing the aspect ratio of the regular finite difference mesh has a visible influence on the lateral propagation of the thermal front with HYDROTHERM. Results from CSMP++ also show that the mesh orientation of the coarse mesh influences the propagation of the front while the mesh refinement in the center part has a minor effect. All simulations still show overall good agreement in the representation of the thermal evolution of the system.

3.2.3. Salt water, two-phase flow

We extended the comparison with TOUGH2 by adding salt to the high-enthalpy fluid source. However, TOUGH2 and CSMP++ treat salt-water source terms differently. In our approach, additional fluids can enter the domain through the source terms $Q_{H_2O+NaCl}$, Q_{NaCl} and Q_a. Assigning a constant source term therefore requires the assignment of an enthalpy for the total fluid, i.e. H_2O + NaCl, and a constant salinity. In order to avoid temperatures exceeding the validity of PetraSim, we assigned a fluid source that initially results in the same temperature as in the pure water example (Figure 10B) by assigning $h_f = 1.3638 \frac{MJ}{kg}$ and $X_f = 0.1$, leading to the source terms $Q_{H_2O+NaCl} = 0.04 \frac{kg}{s}$, $Q_{NaCl} = 0.004 \frac{kg}{s}$ and $Q_a = Q_{H_2O+NaCl} \cdot h_f$ = 54.552 kW.

In the PetraSim version of TOUGH2, a fluid source is applied by assigning a constant flux of additional H_20 and NaCl separately, i.e. there are separate values for the enthalpy of H_2O and NaCl. Here, we define a source term for H_20 as $Q_{H_2O} = 0.036 \frac{kg}{s}$ with an enthalpy of $h_{H_2O} = 1.5 \frac{MJ}{kg}$, and a

source term for NaCl as $Q_{NaCl} = 0.004 \frac{kg}{s}$ with an enthalpy of $h_{NaCl} = 0.138 \frac{MJ}{kg}$, adding up to the same energy source term as $Q_{H_2O} \cdot h_{H_2O} + Q_{NaCl} \cdot h_{NaCl} = 54.552\, kW = Q_a$.

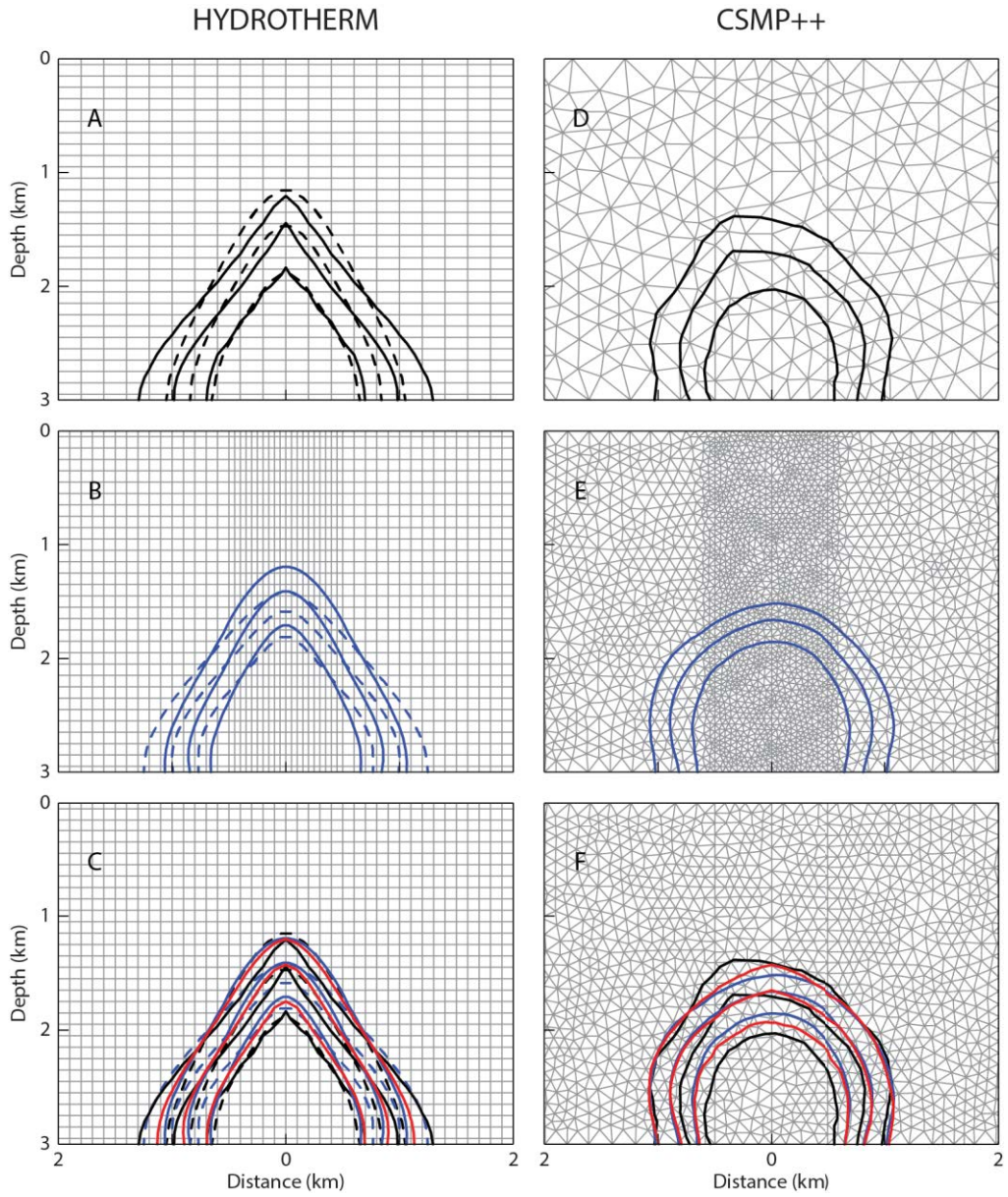

Figure 11. Mesh sensitivity of two-dimensional pure water simulations with the high-enthalpy fluid source (Fig. 10B). The plots show the 100, 200, and 300°C isotherms after 1000 years of simulation time. The bottom panels (**C, F**) show the results from the standard meshes used in this study (Fig. 7) as red lines with the results from the coarser meshes (**A, D**) as black lines and from meshes with a finer central part (**B, E**) as blue lines. The dashed lines show HYDROTHERM results with variations in the vertical resolution instead of the horizontal resolution for coarser (Δy = 200 m, Δx = 100 m; A) and finer (Δy = 50 m, Δx = 100 m; B) meshes (not shown).

Propagation of the thermal front is similar to that with pure water (Figure 11) with TOUGH2 developing a plume shape similar to that of HYDROTHERM, with faster propagation along the center-line. The results of both models generally agree very well at the quasi-steady state, i.e. after the breakthrough of the thermal plume to the surface and after a boiling zone has been established in the upper part of the geometry (Figure 12). Again, the thermal plume calculated with CSMP++ extends slightly further outward than the one calculated with TOUGH2. Phase separation into a low-salinity, low-density vapor phase and a high-salinity, high-density brine starts at a depth of about 1 km (Figure 12).

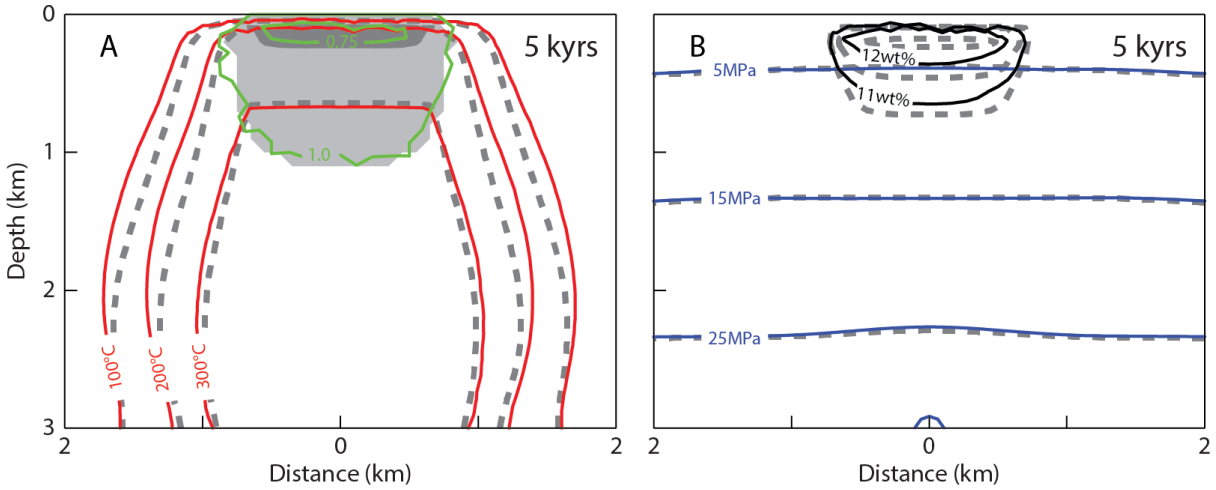

Figure 12. Snapshots of two-phase, two-dimensional simulations with salt water. Results for temperature (red), liquid saturation (green) (A), fluid pressure (blue), and bulk salinity (black) (B) from CSMP++ are plotted as solid lines, results from TOUGH2 as dashed lines (gray). The outer solid green line marks a liquid saturation of 1.0, indicating the extent of the two-phase field; the inner green line shows liquid saturation of 0.75 (**A**). The gray-shaded areas show the respective saturations as calculated by TOUGH2. Increases in bulk salinities are shown as isolines of 11 and 12 wt% NaCl for both simulations (**B**); the 13 wt% NaCl isoline from the TOUGH2 simulation is the center dashed line.

The thermal profile through the central upflow zone for the simulations including high-enthalpy fluid sources, with and without salt, show that the injected fluids ascend at almost constant temperatures in the lower part and follow the boiling curve within the two-phase field in the upper part (Figure 13). Liquid saturations gradually decrease at shallower levels with a low-density, high-enthalpy vapor phase rapidly venting through the surface. In the simulation with salt water, this phase separation leads to an increase in bulk salinity as the high-density, high-salinity brine phase ascends more slowly. With salt, TOUGH2 calculates slightly lower fluid pressures and higher temperatures for the single-phase up-flow zone (Figure 13C). Within the boiling zone, liquid saturations are lower and bulk salinities are higher in the TOUGH2 results as compared to CSMP++ (Figure 13D). However, the results of the two models agree well in general, especially considering the differences in numerical discretization methods and equations of state for the thermodynamic properties of the H_2O-NaCl fluids.

3.2.4. Salt water, multi-phase flow

As a final example, we increase the enthalpy of the input fluid to $h_f = 3.0 \frac{MJ}{kg}$, reduce its salinity to 1 wt% NaCl and repeat the same simulation with three different meshes (Figures 14 and 15). The resulting propagation of a thermal and saline front of magmatic fluids cannot be compared with the two other models used for the benchmarking examples because of its salinity (not applicable for HYDROTHERM) and high temperature (not applicable for TOUGH2).

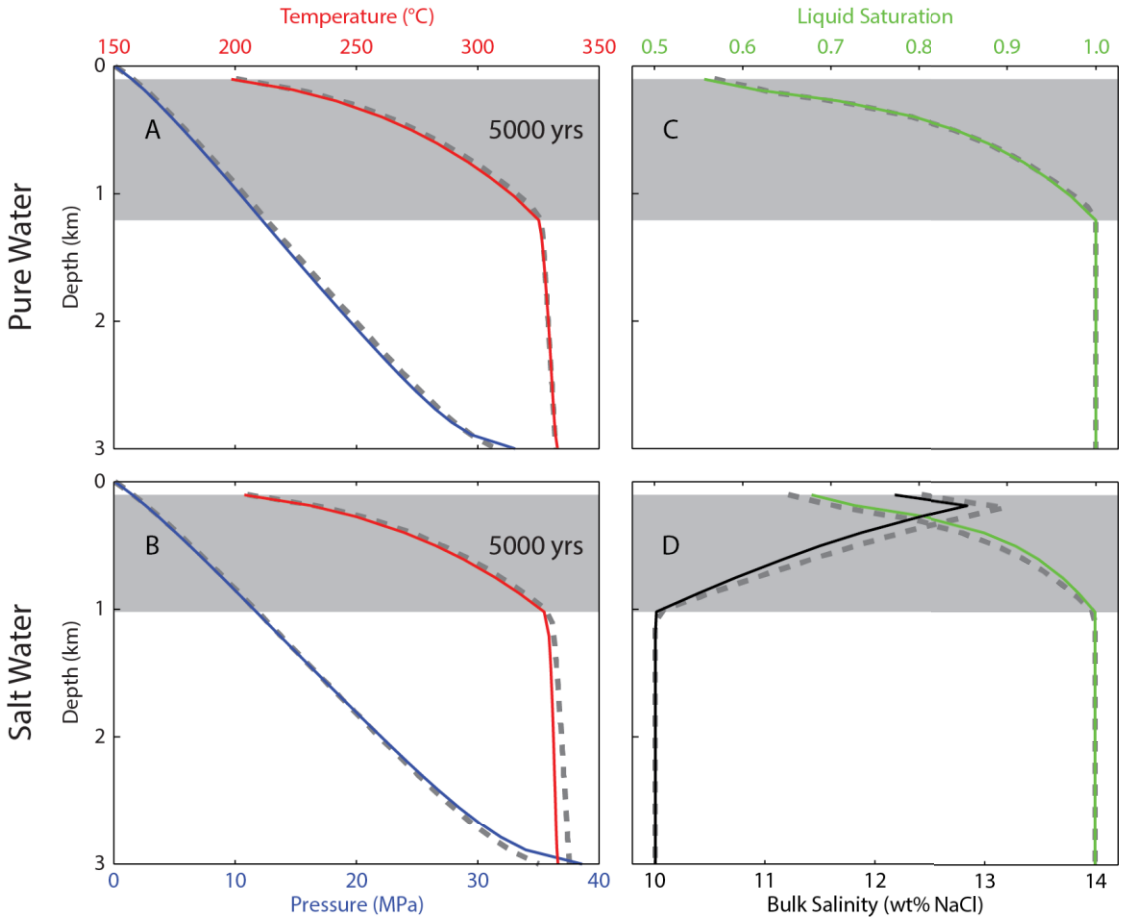

Figure 13. Snapshots along the vertical profile at the center of the two-phase, two-dimensional simulations with (B,D) and without (A,C) salt (Figs 10 and 12). Results for fluid pressure (blue), temperature (red) (**A,B**), liquid saturation (green), and bulk salinity (black) (**C,D**) from CSMP++ are plotted as solid lines, results from TOUGH2 as dashed lines (gray).

In contrast to the two-phase simulations with and without salt shown above, where phase separation happened in the uppermost part of the up-flow zone (Figure 13), here, fluids occur as a two-phase mixture of liquid and vapor above 500°C (Figure15A). The low-density, low-salinity vapor phase physically separates from the high-density, high-salinity liquid, leading to a rapid increase in bulk salinity to values above 30 wt% NaCl at the injection location (Figure 14A). The ascending low-density vapor develops a hot shell of single-phase vapor above and around the two-phase field at the injection point (Figure15A). As in the previous simulations with fluid sources, a fluid pressure anomaly develops to drive away the initial fluids and accommodate the injected fluid mixture. The results obtained for the different mesh resolutions are generally very similar.

Continuing phase separation at depth and decreasing fluid pressures due to breakthrough of the thermal front to the surface lead to saturation of the fluids in solid halite (Figures 14D-F and 15D-F). After 2000 years, the injected two-phase mixture has saturated in halite only a few hundred meters above the injection location. After a brief transition through the three-phase coexistence, fluids enter the two-phase vapor-halite field. At the cooler flanks of this upflow zone, fluids are again in the liquid-vapor coexistence field.

Comparing the results of different mesh resolutions shows that the general patterns such as the thermal profile and the overall distribution of fluid states are the same for all resolutions. However, the system is so dynamic and non-linear that mesh refinement has a visible effect in the details of the results. Only in the finest mesh resolution is the field of three-phase coexistence

(V+L+H) seen to form a continuous ring surrounding the two-phase injection zone (Figure 15F). This transition cannot be resolved with the coarsest mesh (Figure 15E). High bulk salinities are predominant in the lower part of the system and reach values above 70 wt% NaCl as a rim surrounding the injection location. Salinities in the upflow zone only exceed 10 wt% NaCl in the V+L zones flanking the V+H zone in the center. The effect of solid halite on the relative permeability of the mobile phases invokes a pulsating behavior: with decreasing fluid pressure, the hot fluids drop from the V+L field into the V+H field, increasing halite saturation and thereby reducing pore space and permeability. As a result of the blocking effect of solid halite, fluid pressure at the source increases until enough halite is re-dissolved and a batch of fluid can escape to higher levels of the crust.

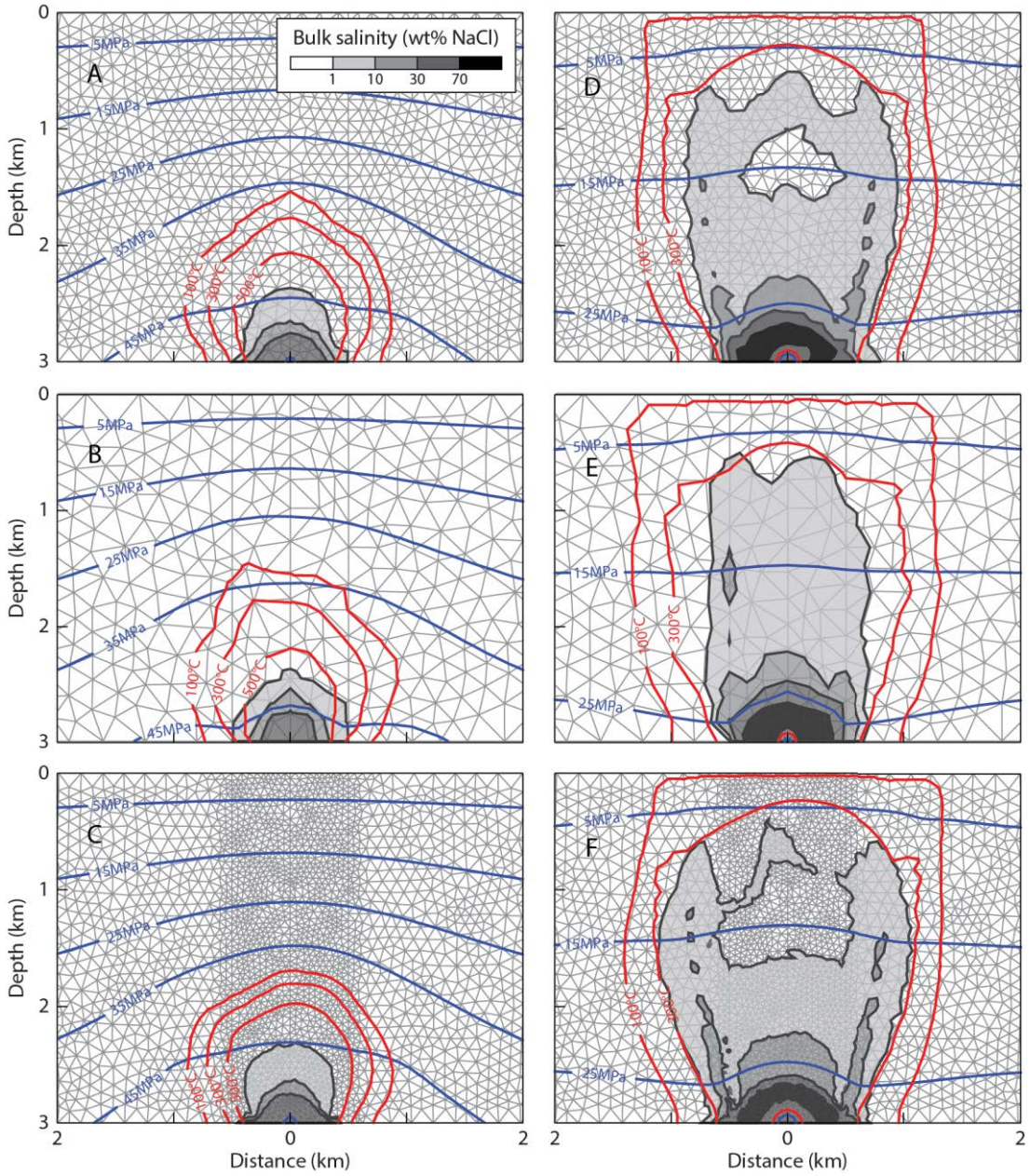

Figure 14. Snapshots of multiphase, two-dimensional simulations with a high-enthalpy salt water source after 500 years (**A–C**) and 2000 years (**D–F**) with standard (**A, D**), coarser (**B, E**), and refined resolution (**C, F**). Results for temperature (red) and fluid pressure (blue) are plotted as solid lines. Increasing bulk salinity is illustrated with the gray-shaded areas.

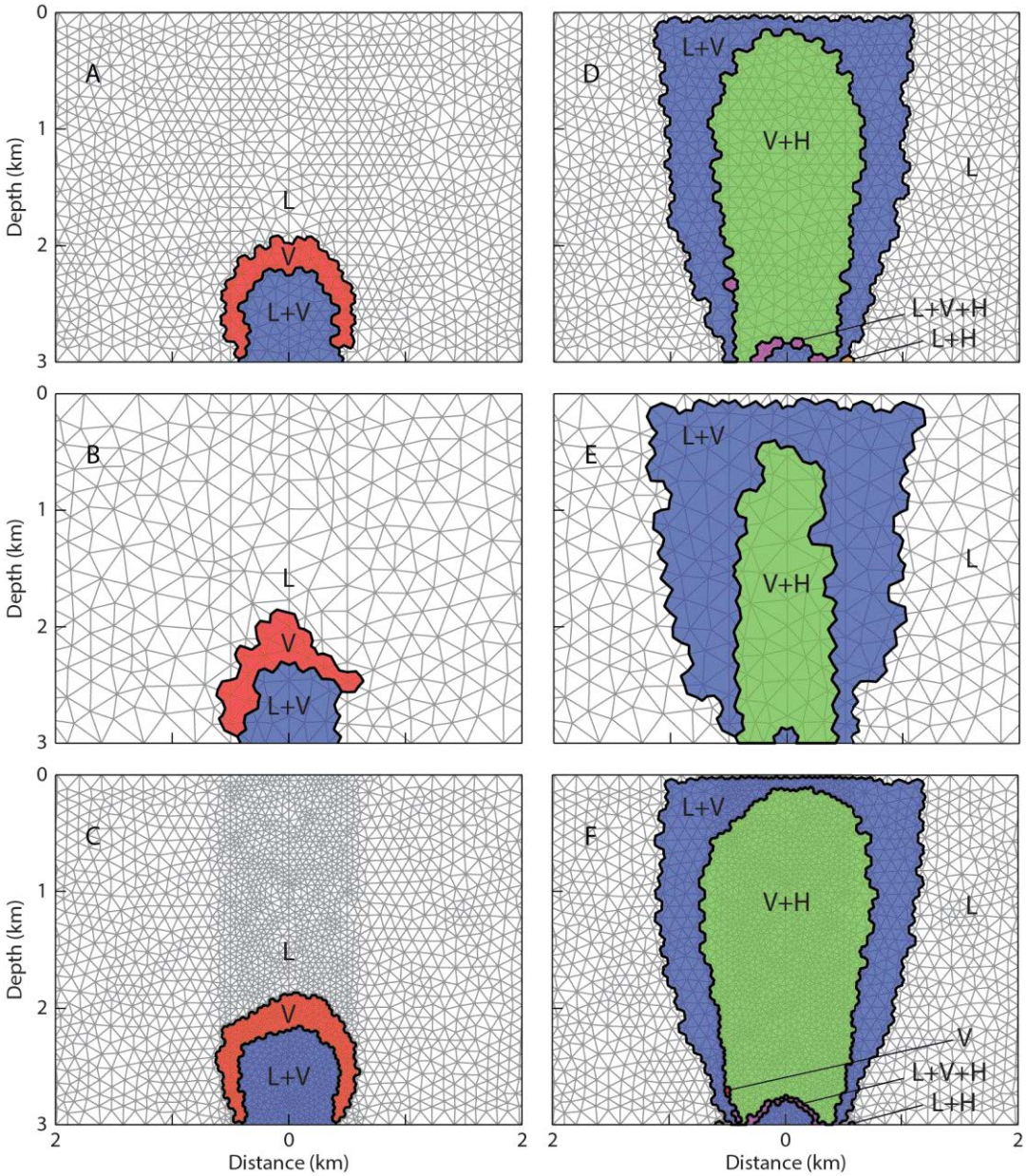

Figure 15. Snapshots of phase relations of two-dimensional simulations with a high-enthalpy salt water source after 500 years (**A–C**) and 2000 years (**D–F**) with standard (**A, D**), coarser (**B, E**), and refined resolution (**C, F**); L = liquid, V = vapor, H = halite.

This pulsating behavior leads to an episodic upward movement of a salt front (Figure 16). Even though the salinity of the fluid source is only 1wt%, bulk salinities rapidly rise to values approaching 100 wt% NaCl, meaning that the pore space is almost entirely filled by solid halite. In Figure 16, the location of the salt front is highlighted with colored solid lines, arrows and shaded areas at 1, 4, 7 and 10 kyrs corresponding to simulations with the standard mesh. These solid lines often plot on top of the dashed lines which indicate intermediate stages. This overlap shows, for example, that the location of the salt front was at roughly the same place between about 5 to 8 kyrs (green area) before it was pushed further to the location marked by the red area (9 and 10 kyrs). At shallower depths above the salt front, bulk salinity only slowly increases with time.

The simulation with the coarser mesh predicts a similar propagation of the salt front (Figure 16B). The main difference between the results with standard and coarse mesh is the front location after 4 kyrs (blue area), indicating that in these simulations the front remained in place for an even

longer period between 4 and 8 kyrs. However, this may also simply be a result of the low resolution, as the extent of the salt front is resolved by only four nodes in the center line of the coarse mesh as compared to eight nodes in the standard mesh. The overall pattern of salt front propagation is captured by the coarse resolution, as indicated by the good agreement of the respective fronts at 10 kyrs.

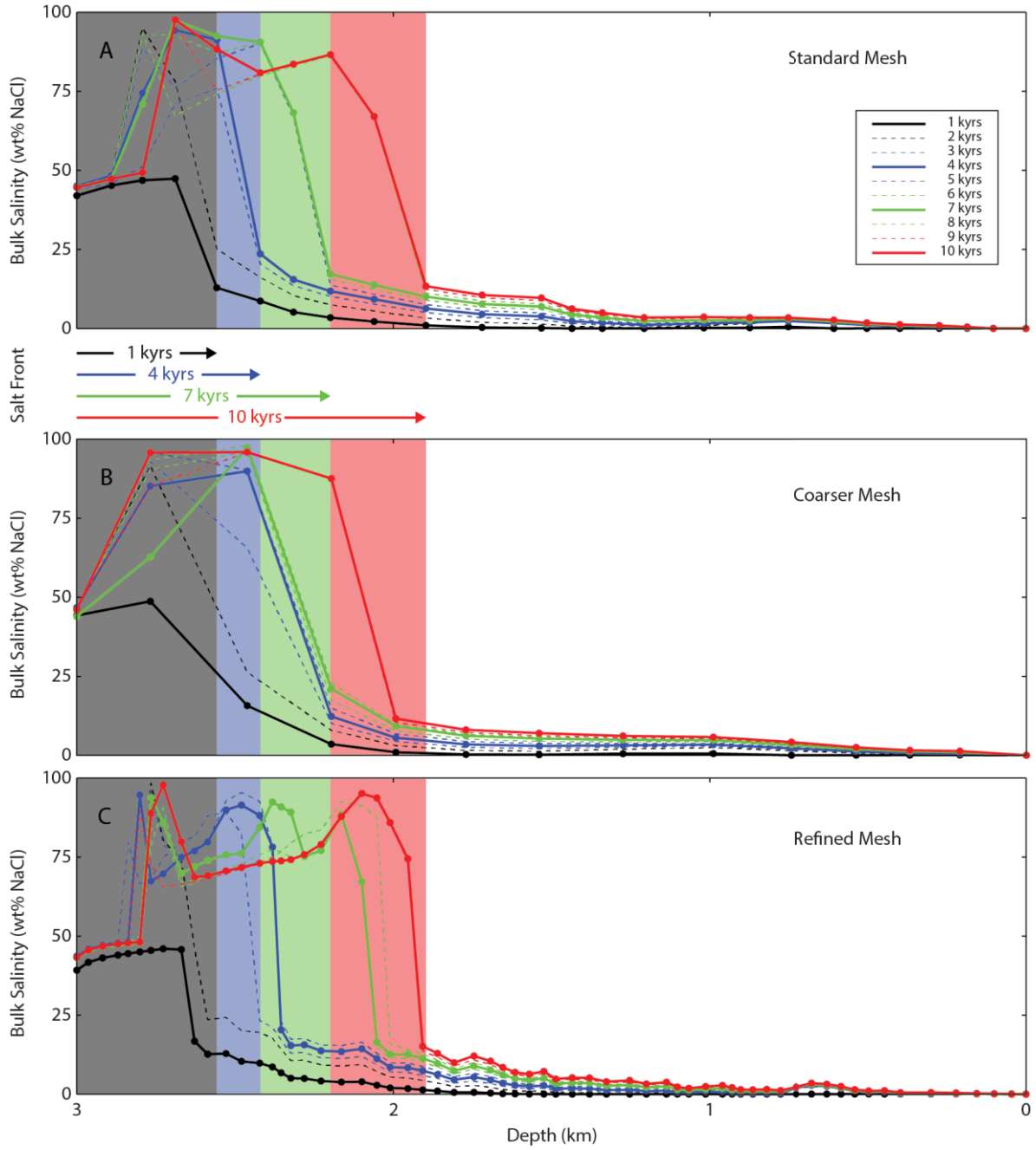

Figure 16. Propagation of the salt front in the two-dimensional simulations with a high-enthalpy salt water source with standard (**A**), coarser (**B**), and refined resolution (**C**) along the vertical profile in the center of the domain. Bulk salinities are plotted with increments of 1000 years as solid or dotted lines with points showing the calculated nodal values. The colored arrows and the shaded areas illustrate the upward propagation of the high-salinity front in time in the standard mesh.

Refining the resolution in the central part of the mesh resolves the propagation of the salt front in more detail (Figure 16C). The fact that some lines still plot on top of each other shows that, even with this fine resolution, the salt front is pushed upwards episodically as a result of the pulsating

behavior of the system. The high-resolution simulation indicates that several salt peaks may develop during the upward propagation. A first high-salinity peak stays relatively constant about 200 to 300 m above the injection point at 3 km depth. Bulk salinities decrease above this first peak and increase again to form a second peak at the actual salt front. The salinity profile after 7 kyrs even shows three salinity peaks, with the middle peak developing latest whereas the outer ones were already in place after 6 kyrs. This middle peak in the high-resolution simulation agrees well with the salt front of the standard-resolution simulation at the same time, whereas the actual salt front has already progressed further upward in the finer resolution mesh (green area). The fronts at 10 kyrs (red area) agree remarkably well between standard and refined meshes, and here the simulation with standard resolution also resolves a two-peak salinity profile (Figure 16A).

Calculating the total salt mass retained in the subsurface in relation to the total salt mass injected into the modeling domain reveals that only a small proportion of the salt added is vented through the surface in the early stages of the system (Figure 17). After a peak at 10% of vented salt at about 1 to 1.5 kyrs, the rate of salt venting first decreases and later slowly increases with time. However, even after 10 kyrs of constant fluid injection, more than three quarters of salt mass added are still retained in the crust. The three different meshes all show the same general trend but vary in the details.

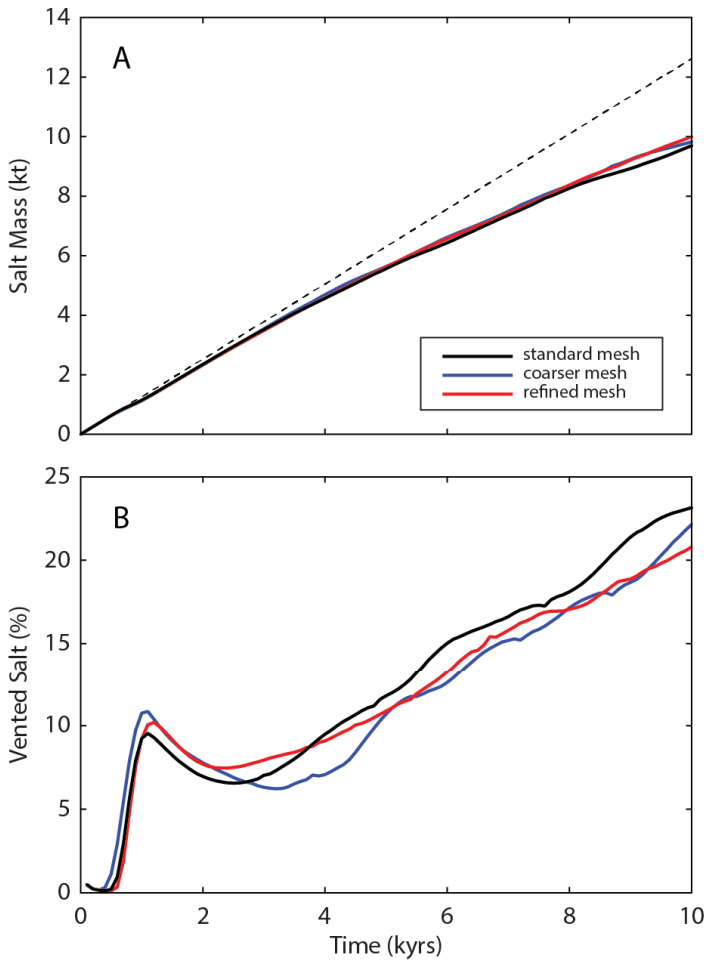

Figure 17. Accumulation of salt mass in the subsurface. (**A**) The temporal evolution of the total mass of salt integrated over the modeling domain with the three different meshes is plotted as solid lines. The total salt mass injected during the simulation is shown by the dashed black line. (**B**) The ratio of salt mass retained in the crust versus the total injected salt mass indicates the percentage of salt mass vented through the top boundary.

4. Discussion

The results from the numerical scheme described here are generally in good to excellent agreement with the results from HYDROTHERM and TOUGH2. All 1D benchmarking examples show almost perfect matches with only minor differences (Figures 4-6). Even simulations with highly non-linear fluid properties, including multi-phase flow and solid halite, yield essentially identical results.

Comparisons of 2D results show that all models predict similar evolution of convecting hydrothermal systems. Differences in the results increase with an increasing degree of non-linear behavior. For systems with comparatively low temperatures, the results of our scheme are in excellent agreement with the results from HYDROTHERM (Figures 8-9). Increasing the temperature leads to larger differences (Figures 10,11 and 13) between CSMP++ and both HYDROTHERM and TOUGH2. Adding salt to the system increases these differences further (Figures 12-13). The equations of state for salt water implemented to TOUGH2 and CSMP++ differ in their details (Pruess 1991; Pruess 2004; Driesner 2007; Driesner and Heinrich 2007), which might explain differences like the deviations in bulk salinity. However, the general pattern of salt-water dynamics is the same for both CSMP++ and TOUGH2.

Contrasting numerical implementation and spatial and temporal discretization of variables may explain other deviations. Differences in the shape of the thermal plume might be related to differences in the spatial and temporal discretization of transient fluid pressure. The CVFEM as applied with CSMP++ calculates pressure gradients that are piecewise constant across a finite element. In contrast, the FD approach taken by HYDROTHERM and TOUGH2 calculates local horizontal and vertical pressure gradients defined by two neighboring nodes. This difference in discretization may explain why the thermal front progresses faster along the middle vertical line compared to CSMP++, while the diagonal progression is faster in CSMP++ and slower in HYDROTHERM and TOUGH2. The dependence of lateral propagation on mesh resolution and aspect ratio of the rectangular elements of HYDROTHERM (Figure 11C) supports this interpretation. The orientation of regular grids has been shown to have a strong effect on fluid flow, with faster front propagation where one direction of the grid is orientated parallel to the main direction of flow (Huber and Helmig 1999; Huber and Helmig 2000; Kozdon et al. 2008).

As the differences increase with increasingly non-linear fluid properties at higher temperatures, the discretization of fluid properties in space and time is also likely to play a role. While CSMP++ always uses fluid properties from the upwind node, HYDROTHERM interpolates some properties onto the midpoints, such as viscosity and density, while others are taken at the upstream node, such as enthalpies and relative permeabilities. The slightly faster advance of the thermal front in the pure-water two-phase example in vertical orientation could be related to this difference in spatial discretization of fluid density (Figure 5C-D); small differences in density will impact the gravity component and hence rate of vertical flow. We observe that the horizontal example shows a perfect match of the thermal fronts (Figure 5A-B). Another factor that impacts the small differences observed in the results could be that HYDROTHERM uses fluid properties at the next time level and allows for larger time-steps, and hence introduced more numerical dispersion, while CSMP++ uses the properties at the current time level and smaller time steps with less numerical dispersion. These factors are also likely to affect the shape of the thermal front. The same holds for TOUGH2, which also uses a fully-coupled, fully-implicit, and hence iterative time-stepping approach that allows for larger time steps at the expense of increased numerical

dispersion. Despite these deviations, the general pattern of the hydrothermal systems is always in good agreement for all three numerical models.

The final example illustrates that the complexity of the full range of phase relations of the H_2O-NaCl system for magmatic-hydrothermal conditions can lead to heterogeneities within the modeling domain even when a static, uniform permeability is invoked (Figure 14-17). Effects of mesh orientation can already be observed with increasingly non-linear behavior of the fluid properties, e.g. in the example with high heat flux (Figure 10A) where the thermal plume in the unstructured mesh as calculated with CSMP++ has a slight tendency towards the left side as compared to the results from HYDROTHERM which is obtained on a perfectly symmetric finite difference grid. Also, the mesh dependency of the shape of the plume in the results from HYDROTHERM increase with increasing temperatures (Figures 9C and 11C).

These effects are even stronger when solid halite is precipitating, because of its immediate influence on the remaining available permeability for the liquid and vapor phases. However, one remarkable result is that even the coarsest resolution is able to capture the large-scale dynamics of the fluid plume and the propagation of the salt front (Figure 14). On the other hand, the hydrothermal system under these extreme conditions is so dynamic that mesh refinement in the inner part of the domain has a visible effect on the results. With the finest mesh, the upflow zone becomes more dynamic, leading to slightly higher temperatures and slightly lower salinities at the right side of the center line, as is illustrated by the discontinuity in the 10 wt% salinity field at 1 km depth (Figure 14F). Similar impacts of the mesh resolution have been shown for dynamic convection systems with pure water (e.g. Coumou et al. 2006).

The final example further demonstrates the influence of phase-separation of saline fluids within the crust. Even though we chose a moderate salinity of 1 wt% NaCl for the magmatic volatiles, the hydrothermal system is unable to transport most of the salt to the upper parts of the domain or through the surface (Figure 17). Only small corridors of liquid-vapor coexistence at the flanks of a large central vapor-halite field manage to move saline fluids upward. Most of the salt is precipitated as solid halite when the hot saline liquid-vapor mixture enters the vapor-halite field with a decrease in fluid pressure during ascent (see Figure 1 for phase relations) and can only episodically be pushed further upward in pulses (Figure 16).

Such non-linear behavior cannot be resolved with approximations or dimensionless numbers that require a steady-state convection pattern but has to be resolved with transient numerical calculations. The CFL- and mass-based time step criteria required within the presented scheme can have a significant effect on computation time, especially when very fine meshes are used. This constraint requires that for every simulation, the level of detail that is needed or desired has to be evaluated when constructing the modeling domain and mesh. If high-resolution meshes are needed to capture the dynamics, parallel techniques implemented in CSMP++ using the message passing interface (MPI) may help to keep computational time acceptable (Coumou et al. 2008c).

In general, the results presented in this study suggest that the amount of magmatic salt added to hydrothermal system is not easily accommodated or flushed out of the subsurface. The blocking effect of the solid halite phase may be overestimated in the 2D simulation performed for this study because the radial outward propagation can disperse some salt into the third dimension, i.e. the high-salinity ring around the injection point (Figure 14) would become a rounded cap in 3D. Also, some solid salt might be carried with the upward-streaming fluids, though this effect is likely to be small if halite coexists with a low-density vapor phase. The results suggest that this halite

phase might be a very significant component of magmatic-hydrothermal systems, at least temporarily. The effect might be overlooked as solid halite is rarely or only indirectly documented by fluid inclusions (Cloke and Kesler 1979; Muntean and Einaudi 2000). Conceptual hydrological models for salt water systems should therefore take into account the amount of salt added to the system, either by quantitative mass-balance calculations or by testing hydrological concepts with numerical simulations.

5. Conclusions

We developed a new numerical scheme for simulations of thermohaline convection at magmatic-hydrothermal conditions based on the Control Volume Finite Element Method (CVFEM). The scheme incorporates an accurate module for phase states and fluid properties of salt water and was tailored to ensure stable solutions for extreme conditions in concert with large fluid source terms as might arise in crustal settings where magmatic volatiles are released into the subsurface hydrosphere. We found that avoiding interpolation or averaging of fluid properties is key for the stability of the numerical scheme, which motivated conversion from a FEFV to a CVFEM approach.

In a series of one- and two-dimensional benchmarking examples with and without salt, we compared our results with two well-established models, HYDROTHERM and TOUGH2, and found good to excellent agreement. With increasingly non-linear fluid behavior, the different numerical approaches start to exhibit differences in the detail, while the general patterns continue to show good agreement between simulations.

These non-linearities can result in highly dynamic and unexpected behavior, which is illustrated in a final example under high-temperature, high-salinity conditions currently outside of the range for the two other models. Here, precipitation of solid halite introduces heterogeneities to the system which influence the fluid dynamics. While mesh orientation and resolution have an effect in the detailed picture, the general, larger-scale pattern can be captured by a relatively coarse mesh.

This scheme and its precursors have shown how important an accurate treatment of multi-phase H_2O-NaCl fluids is for providing insights into a range of Earth science questions. For example, the formation of heat-pipes under two-phase flow conditions can strongly increase energy transport within mid-ocean ridge hydrothermal systems (Coumou et al. 2008a). Further, the large range in observed vent fluid salinities at black smoker fields can be explained by brine-vapor dynamics in the subsurface (Coumou et al. 2009) with system-scale permeability controlling venting temperatures and salinities (Driesner 2010). Simulations of the hydrology of Brothers volcano in the Kermadec arc, New Zealand, revealed that a source of magmatic fluids is required to explain venting behavior of this active submarine arc volcano (Gruen et al. 2012). The interplay of a dynamic permeability model describing the brittle-ductile transition and hydraulic fracturing driven by expulsion of saline magmatic volatiles from a cooling magma chamber results in a hydrological divide that stabilizes copper precipitation in ore shells of porphyry deposits (Weis et al. 2012). This divide separates a magmatic fluid plume at high temperatures and near-lithostatic fluid pressures from cooler meteoric fluids convecting under near-hydrostatic pressures and may also be a pre-requisite for so-called supercritical geothermal systems (Weis and Driesner 2013). Generic simulations with low-salinity, high-enthalpy magmatic fluids in this study show that salt is not easily flushed through the system and that precipitation of solid halite can cause episodic fluid fluxes even with a steady rate of fluid supply and constant, homogeneous rock properties.

The numerical method will also allow us to implement additional fluid-rock interactions due to chemical reactions or rock mechanics, such as might be required to characterize enhanced geothermal systems or carbon storage in the subsurface. Modeling reactive transport also requires that fluid properties be evaluated at the location of thermal and chemical equilibration, as interpolations and averaging are unlikely to represent physically and chemically meaningful fluid or rock properties. Heterogeneity effects similar to those described for solid halite in this study are likely to become even stronger with additional interplay of fluid flow, rock mechanics and chemistry.

Acknowledgments

Many thanks to Steve Ingebritsen and Warwick Kissling for their reviews, which were particularly helpful to round up the manuscript. We are very grateful to the CSMP++ community of developers and users for code developments, discussions and collaborations during the last years, in particular S.K. Matthäi, G. Grün, I. Steinberger, S.J. Fowler, S. Scott, K. Schmid, Y. Zaretzkiy, R. Annewandter, C. Maier, A. Paluszny, H. Nick and J. Mindel. The authors also greatly thank C.A. Heinrich for his long-term active support for this numerical tool and its development which took several generations of researchers. The work has been supported by the Swiss National Science Foundation within various funding periods.

References

Aavatsmark I (2002) An introduction to multipoint flux approximations for quadrilateral grids. *Computational Geosciences*, 6, 405-432.

Annewandter R, Main I & Geiger S (2013) High-resolution numerical simulations of capillary trapping of carbon dioxide in fractured formations. SPE Paper SPE-166002. In: SPE Reservoir Characterisation and Simulation Conference and Exhibition, September 16-18, Abu Dhabi, U.A.E. Society of Petroleum Engineers, 1-21. http://dx.doi.org/10.2118/166002-MS

Bani-Hassan N, Iyer K, Rupke LH & Borgia A (2012) Controls of bathymetric relief on hydrothermal fluid flow at mid-ocean ridges. *Geochemistry Geophysics Geosystems*, 13, doi: 10.1029/2012gc004041.

Brooks RH & Corey AT (1964) Hydraulic properties of porous media. *Hydrological Papers*, Vol. 3 Colorado State University, USA, 107-116.

Cathles LM (1977) An analysis of the cooling of intrusives by ground-water convection which includes boiling. *Economic Geology*, 72, 804-826.

Cline JS & Bodnar RJ (1991) Can economic porphyry copper mineralization be generated by a typical calc-alkaline melt. *Journal of Geophysical Research-Solid Earth and Planets*, 96, 8113-8126.

Cloke PL & Kesler SE (1979) Halite trend in hydrothermal solutions. *Economic Geology*, 74, 1823-1831.

Connolly JAD & Podladchikov YY (2004) Fluid flow in compressive tectonic settings: Implications for midcrustal seismic reflectors and downward fluid migration. *Journal of Geophysical Research-Solid Earth*, 109, B04201, doi: 10.1029/2003jb002822.

Coumou D (2008) Numerical simulation of fluid flow in mid-ocean ridge hydrothermal systems. PhD thesis, ETH Zurich, Switzerland, p. 163.

Coumou D, Driesner T, Geiger S, Heinrich CA & Matthai S (2006) The dynamics of mid-ocean ridge hydrothermal systems: Splitting plumes and fluctuating vent temperatures. *Earth and Planetary Science Letters*, 245, 218-231.

Coumou D, Driesner T & Heinrich CA (2008a) Heat transport at boiling, near-critical conditions. *Geofluids*, 8, 208-215.

Coumou D, Driesner T & Heinrich CA (2008b) The structure and dynamics of mid-ocean ridge hydrothermal systems. *Science*, 321, 1825-1828.

Coumou D, Driesner T, Weis P & Heinrich CA (2009) Phase separation, brine formation, and salinity variation at Black Smoker hydrothermal systems. *Journal of Geophysical Research-Solid Earth*, 114, B03212, doi: 10.1029/2008jb005764.

Coumou D, Matthai S, Geiger S & Driesner T (2008c) A parallel FE-FV scheme to solve fluid flow in complex geologic media. *Computers & Geosciences*, 34, 1697-1707.

Cox SF (2005) Coupling between Deformation, Fluid Pressures, and Fluid Flow in Ore-Producing Hydrothermal Systems at Depth in the Crust. *Economic Geology*, 100th Anniversary Volume, 39-75.

Driesner T (2007) The system H2O-NaCl. Part II: Correlations for molar volume, enthalpy, and isobaric heat capacity from 0 to 1000 degrees C, 1 to 5000 bar, and 0 to 1 X-NaCl. *Geochimica Et Cosmochimica Acta*, 71, 4902-4919.

Driesner T (2010) The interplay of permeability and fluid properties as a first order control of heat transport, venting temperatures and venting salinities at mid-ocean ridge hydrothermal systems. *Geofluids*, 10, 132-141.

Driesner T & Geiger S (2007) Numerical simulation of multiphase fluid flow in hydrothermal systems. In: *Fluid-Fluid Interactions* (eds Liebscher A & Heinrich CA) Chantilly, Mineralogical Soc Amer, 65, 187-212.

Driesner T & Heinrich CA (2007) The system H2O-NaCl. Part I: Correlation formulae for phase relations in temperature-pressure-composition space from 0 to 1000 degrees C, 0 to 5000 bar, and 0 to 1 X-NaCl. *Geochimica Et Cosmochimica Acta*, 71, 4880-4901.

Edwards MG (2006) Higher-resolution hyperbolic-coupled-elliptic flux-continuous CVD schemes on structured and unstructured grids in 2-D. *International Journal for Numerical Methods in Fluids*, 51, 1059-1077.

Evans KF, Genter A & Sausse J (2005) Permeability creation and damage due to massive fluid injections into granite at 3.5 km at Soultz: 1. Borehole observations. *Journal of Geophysical Research-Solid Earth*, 110, B04203, doi: 10.1029/2004jb003168.

Fairley JP, Ingebritsen SE & Podgorney RK (2010) Challenges for Numerical Modeling of Enhanced Geothermal Systems. *Ground Water*, 48, 482-483.

Faust CR & Mercer JW (1979) Geothermal reservoir simulation. 1. Mathematical models for liquid-dominated and vapor-dominated hydrothermal systems. *Water Resources Research*, 15, 23-30.

Fontaine FJ, Rabinowicz M & Boulegue J (2001) Permeability changes due to mineral diagenesis in fractured crust: implications for hydrothermal circulation at mid-ocean ridges. *Earth and Planetary Science Letters*, 184, 407-425.

Forsyth PA (1991) A control volume finite-element approach to NAPL groundwater contamination. *Siam Journal on Scientific and Statistical Computing*, 12, 1029-1057.

Fournier RO (1991) The transition from hydrostatic to greater than hydrostatic fluid pressure in presently active continental hydrothermal systems in crysalline rock. *Geophysical Research Letters*, 18, 955-958.

Fournier RO (1999) Hydrothermal processes related to movement of fluid from plastic into brittle rock in the magmatic-epithermal environment. *Economic Geology and the Bulletin of the Society of Economic Geologists*, 94, 1193-1211.

Fritz J, Flemisch B & Helmig R (2012) Decoupled and multiphysics models for non-isothermal compositional two-phase flow in porous media. *International Journal of Numerical Analysis and Modeling*, 9, 17-28.

Geiger S, Driesner T, Heinrich CA & Matthai SK (2006a) Multiphase thermohaline convection in the earth's crust: I. A new finite element - Finite volume solution technique combined with a new equation of state for NaCl-H2O. *Transport in Porous Media*, 63, 399-434.

Geiger S, Driesner T, Heinrich CA & Matthai SL (2006b) Multiphase thermohaline convection in the earth's crust: II. Benchmarking and application of a finite element - finite volume solution technique with a NaCl-H2O equation of state. *Transport in Porous Media*, 63, 435-461.

Geiger S, Matthai S, Niessner J & Helmig R (2009) Black-Oil Simulations for Three-Component, Three-Phase Flow in Fractured Porous Media. *SPE Journal*, 14, 338-354, doi:10.2118/107485-PA.Geiger S, Robert S, Matthai SK, Zoppou C & Burri A (2004) Combining finite element and finite volume methods for efficient multiphase flow simulations in highly heterogeneous and structurally complex geologic media. *Geofluids*, 4, 284-299.

Gerritsen MG & Durlofsky LJ (2005) Modeling fluid flow in oil reservoirs. *Annual Review of Fluid Mechanics*, 37, 211-238.

Grant MA & Sorey ML (1979) Compressibility and hydraulic diffusivity of a water-steam flow. *Water Resources Research*, 15, 684-686.

Gruen G, Weis P, Driesner T, de Ronde CEJ & Heinrich CA (2012) Fluid-Flow Patterns at Brothers Volcano, Southern Kermadec Arc: Insights from Geologically Constrained Numerical Simulations. *Economic Geology*, 107, 1595-1611.

Gunnarsson G, Arnaldsson A & Oddsdottir AL (2011) Model Simulations of the Hengill Area, Southwestern Iceland. *Transport in Porous Media*, 90, 3-22.

Haar L, Gallagher JS & Kell GS (1984) *NBS/NRC Steam Tables: Thermodynamic and transport properties and computer programs for vapor and liquid states of water in SI units*. Hemisphere Publishing Corporation, Washington, New York,London, pp. 320.

Halbach P, Tunnicliffe V & Hein JR (2003) *Energy and Mass Transfer in Marine Hydrothermal Systems*. Berlin, Dahlem University Press, pp. 365.

Hanson RB (1995) The hydrodynamics of contact-metamorphism. *Geological Society of America Bulletin*, 107, 595-611.

Hayba DO & Ingebritsen SE (1997) Multiphase groundwater flow near cooling plutons. *Journal of Geophysical Research*, 102, 12235-12252.

Helmig R, Flemisch B, Wolff M, Ebigbo A & Class H (2013) Model coupling for multiphase flow in porous media. *Advances in Water Resources*, 51, 52-66.

Huber R & Helmig R (1999) Multiphase flow in heterogeneous porous media: A classical finite element method versus an implicit pressure explicit saturation-based mixed finite element finite volume approach. *International Journal for Numerical Methods in Fluids*, 29, 899-920.

Huber R & Helmig R (2000) Node-centered finite volume discretizations for the numerical simulation of multiphase flow in heterogeneous porous media. *Computational Geosciences*, 4, 141-164.

Ingebritsen SE, Geiger S, Hurwitz S & Driesner T (2010) Numerical Simulation of Magmatic Hydrothermal Systems. *Reviews of Geophysics*, 48, RG1002, doi: 10.1029/2009RG000287.

Ingebritsen SE, Sanford S & Neuzil C (2006) *Groundwater in Geologic Processes*, 2nd edn., Cambridge University Press, pp. 536.

Iyer K, Rupke LH & Morgan JP (2010) Feedbacks between mantle hydration and hydrothermal convection at ocean spreading centers. *Earth and Planetary Science Letters*, 296, 34-44.

Keating GN, Geissman JW & Zyvoloski GA (2002) Multiphase modeling of contact metamorphic systems and application to transitional geomagnetic fields. *Earth and Planetary Science Letters*, 198, 429-448.

Kesler SE (1994) *Mineral resources, economics and the environment*. Macmillan Publishing Co, New York, pp. 391.

Ketilsson J, Podgorney R, Driesner T & Regenauer-Lieb K (2012) International Partnership for Geothermal Technology: Geothermal Reservoir Modeling - Recommendations for Research and Development. *IPGT Reservoir Modeling White Paper*, http://www.internationalgeothermal.org/Working_Groups/Modeling.html.

Kipp Jr. KL, Hsieh PA & Charlton SR, (2008) Guide to the Revised Ground-Water Flow and Heat Transport Simulator: HYDROTHERM -- Version 3. *Techniques and Methods,* US Geological Survey, Reston, Va, USA, 6-A25, pp. 160.

Kissling WM (2005a) Transport of three-phase hyper-saline brines in porous media: Examples. *Transport in Porous Media*, 60, 141-157.

Kissling WM (2005b) Transport of three-phase hyper-saline brines in porous media: Theory and code implementation. *Transport in Porous Media*, 61, 25-44.

Kozdon J, Gerritsen M & Christie M (2008) Grid orientation revisited: Near-well, early-time effects and solution coupling methods. *Transport in Porous Media*, 73, 255-277.

Lewis KC & Lowell RP (2009) Numerical modeling of two-phase flow in the NaCl-H2O system: Introduction of a numerical method and benchmarking. *Journal of Geophysical Research-Solid Earth*, 114, doi: 10.1029/2008jb006029.

Lie KA, Krogstad S, Ligaarden IS, Natvig JR, Nilsen HM & Skaflestad B (2012) Open-source MATLAB implementation of consistent discretisations on complex grids. *Computational Geosciences*, 16, 297-322.

Lupi M, Geiger S & Graham CM (2011) Numerical simulations of seismicity-induced fluid flow in the Tjornes Fracture Zone, Iceland. *Journal of Geophysical Research-Solid Earth*, 116.

Matthai SK, Geiger S, Roberts SG, Paluszny A, Belayneh M, Burri A, Mezentsev A, Lu H, Coumou D, Driesner T & Heinrich CA (2007) Numerical simulation of multi-phase fluid flow in structurally complex reservoirs. In: *Structurally Complex Reserviors* (eds Jolley SJ, Barr D, Walsh JJ & Knipe RJ) The Geological Society, London, 292, 405-429.

Muntean JL & Einaudi MT (2000) Porphyry gold deposits of the Refugio district, Maricunga belt, northern Chile. *Economic Geology*, 95, 1445-1472.

Norton D & Knight J (1977) Transport phenomena in hydrothermal systems: Cooling plutons. *American Journal of Science*, 277, 937-981.

Pruess K (1991) TOUGH2 – A general-purpose numerical simulator for multiphase fluid and heat flow. Report LBL-29400, Lawrence Berkeley Natl. Lab., Berkeley, CA, USA, doi: 10.2172/5212064.Pruess K (2004) The TOUGH codes - A family of simulation tools for multiphase flow and transport processes in permeable media. *Vadose Zone Journal*, 3, 738-746.

Rice JR (1992) Fault stress states, pore pressure distributions, and the weakness of the San Andreas Fault. In: *Fault Mechanics and Transport Properties of Rocks* (ed. Evans B, Wong, T.F.), Academic Press, New York, 51, 475–475.

Rojstaczer SA, Ingebritsen SE & Hayba DO (2008) Permeability of continental crust influenced by internal and external forcing. *Geofluids*, 8, 128-139.

Rusk BG, Reed MH, Dilles JH, Klemm L & Heinrich CA (2004) Compositions of magmatic hydrothermal fluids determined by LA-ICP-MS of fluid inclusions from the porphyry copper-molybdenum deposit at Butte, MT. *Chemical Geology*, 210, 173-199.

Sammel EA, Ingebritsen SE & Mariner RH (1988) The hydrothermal system at Newberry Volcano, Oregon. *Journal of Geophysical Research-Solid Earth and Planets*, 93, 10149-10162.

Schmid KS, Geiger S & Sorbie KS (2013) Higher order FE-FV method on unstructured grids for transport and two-phase flow with variable viscosity in heterogeneous porous media. *Journal of Computational Physics*, 241, 416-444.

Shewchuk JR (2002) Delaunay refinement algorithms for triangular mesh generation. *Computational Geometry*, 22, 21-74.

Sibson RH (1992) Implications of fault-valve behavior for rupture nucleation and recurrence. *Tectonophysics*, 211, 283-293.

Steele-Maclnnis M, Han L, Lowell RP, Rimstidt JD & Bodnar RJ (2012) The role of fluid phase immiscibility in quartz dissolution and precipitation in sub-seafloor hydrothermal systems. *Earth and Planetary Science Letters*, 321, 139-151.

Stein CA & Stein S (1994) Constraints on hydrothermal heat-flux through the oceanic lithosphere from global heat-flow. *Journal of Geophysical Research*, 99, 3081-3095.

Stüben K (2001) An Introduction to Algebraic Multigrid. In: *Multigrid* (ed. Trottenberg U, Oosterlee CW & Schüller A), Academic Press, 413-532.

Taron J, Elsworth D & Min KB (2009) Numerical simulation of thermal-hydrologic-mechanical-chemical processes in deformable, fractured porous media. *International Journal of Rock Mechanics and Mining Sciences*, 46, 842-854.

Trangenstein JA & Bell JB (1989) Mathematical structure of compositional reservoir simulation. *Siam Journal on Scientific and Statistical Computing*, 10, 817-845.

Voller VR (2009) *Basic Control Volume Finite Element Methods for Fluids and Solids*. World Scientific Publishing Co. Pte. Ltd., Singapore, pp. 170.

Wang CT & Horne RN (2000) Boiling flow in a horizontal fracture. *Geothermics*, 29, 759-772.

Weis P & Driesner T (2013) The interplay of non-static permeability and fluid flow as a possible pre-requisite for supercritical geothermal resources. *Energy Procedia*, 40, 102 - 106.

Weis P, Driesner T & Heinrich CA (2012) Porphyry-Copper Ore Shells Form at Stable Pressure-Temperature Fronts Within Dynamic Fluid Plumes. *Science*, 338, 1613-1616.

Weis P, Thomas M & Sundermann J (2008) Broad frequency tidal dynamics simulated by a high-resolution global ocean tide model forced by ephemerides. *Journal of Geophysical Research-Oceans*, 113, C10029, doi: 10.1029/2007jc004556.